



HAL
open science

Mode I delamination R-Curve in poplar laminated veneer lumber

Axel Peignon, Joël Serra, L. Gélard, Arthur Cantarel, Florent Eyma, B. Castanié

► **To cite this version:**

Axel Peignon, Joël Serra, L. Gélard, Arthur Cantarel, Florent Eyma, et al.. Mode I delamination R-Curve in poplar laminated veneer lumber. Theoretical and Applied Fracture Mechanics, 2023, 10.1016/j.tafmec.2023.103982 . hal-04141431v2

HAL Id: hal-04141431

<https://hal.science/hal-04141431v2>

Submitted on 25 Aug 2023

HAL is a multi-disciplinary open access archive for the deposit and dissemination of scientific research documents, whether they are published or not. The documents may come from teaching and research institutions in France or abroad, or from public or private research centers.

L'archive ouverte pluridisciplinaire **HAL**, est destinée au dépôt et à la diffusion de documents scientifiques de niveau recherche, publiés ou non, émanant des établissements d'enseignement et de recherche français ou étrangers, des laboratoires publics ou privés.

Mode I delamination R-Curve in poplar laminated veneer lumber

A. Peignon¹, J. Serra¹, L. Gélard¹, A. Cantarel¹, F. Eyma¹ and B. Castanié^{1,*}

¹Institut Clément (ICA), Université de Toulouse, CNRS UMR 5312, INSA, ISAE-Supaéro, INSA, IMT Mines Albi, UPS, Toulouse, France

*corresponding author: bruno.castanie@insa-toulouse.fr

Abstract: Recent studies have shown that plywood and laminated veneer lumber are very efficient crashworthiness materials. Therefore, there is a need to determine the fracture toughness of these wood composite materials to be able to model their static and dynamic damage behavior. This study reports the results of the delamination propagation of plywood under mode I loading. Two different double cantilever beam specimens made of poplar were compared: one with an interfacial fiber orientation of 0°/0° and the second with 0°/90°. Failure scenarios and patterns are analyzed to establish a comparison between the two configurations and compute consistent R-curves.

Keywords: Wood veneers, R-curve, Double Cantilever Beam (DCB), Delamination, Fiber bridging, Laminated veneer lumber (LVL)

Funding: This work was supported by the French National Research Agency under the BOOST project (ANR-21-CE43-0008-01).

CC: Compliance Calibration
DCB: Double Cantilever Beam
IR: InfraRed
LVL: Laminated Veneer Lumber
MBT: Modified Beam Theory
MCC: Modified Compliance Calibration
RSD: Relative Standard Deviation
SEA: Specific Energy Absorption
SD: Standard Deviation

17 Nomenclature

a	crack length
a_0	initial crack length
b	specimen width
C	specimen compliance
E_L	modulus of elasticity of wood along the longitudinal direction
G_{Ic}	fracture toughness in mode I
h	specimen height
I	moment of inertia of a DCB specimen arm
L	veneer longitudinal direction
L'	half width of loading block
l	specimen length
P	load acting on the specimen
R	veneer Radial direction
T	veneer Tangential direction
t	distance from loading block pin to center line of top specimen arm
X	specimen length direction
x_0	x coordinate of the crack origin
x_1	x coordinate of point 1
x_f	x coordinate of crack tip
Y	specimen depth direction
y_0	y coordinate of crack origin
y_1	y coordinate of point 1
y_f	y coordinate of crack tip
Z	specimen thickness direction
δ	applied displacement
λ_i	i-th coefficient of an unknown function

18

19 **1. Introduction**

20 Wood is one of the earliest materials used by man in construction [1]. It is a well-known material for
21 which there exists fairly detailed knowledge of its pathologies and durability characteristics. One of
22 the first building codes concerned wood as the material and was published in 1091 in China [2].
23 Wood, especially used in sandwich structures, was also one of the materials used in aeronautics in its
24 early days and until the Second World War [3]. In addition, it is a natural and renewable material,
25 which can be produced locally and recycled [4], [5]. It also acts as a carbon sink, a natural reservoir
26 capable of absorbing and storing carbon from atmospheric CO₂. Wood can therefore play a key role in
27 the fight against global warming [6]. Its waste products are also reusable as a secondary material or
28 energy source [7] and structural material [8].

29 Laminated veneer lumber (LVL) and plywood are structural composite products made from thin,
30 peeled wood plies, called veneers, assembled with an adhesive. Plywood has cross-lamination, which
31 means that longitudinal and transverse veneers are alternated throughout the laminate [9]. Because of
32 their manufacturing steps, LVL and plywood offer the possibility of selecting veneers without visible
33 defects such as knots, knotholes or cracks and have static mechanical characteristics comparable to, or
34 even superior to, those of solid wood [10]–[13]. In addition, recent studies by the authors have shown
35 that LVL also has interesting mechanical potential for crash or impact applications [14]–[18]. For
36 example, Guélou et al. [14] obtained a dynamic Specific Energy Absorption (SEA) for birch wood
37 ranging between 35.7 J/g and 41.1 J/g. The SEA refers to the amount of energy per gram that a
38 material can absorb before it fails or breaks. In addition, sandwich structures with plywood cores and
39 composite (glass, carbon, linen) or metal (aluminium) skins [19], have shown very good resistance to
40 low-speed/low-energy impact [20] as well as excellent post-impact compressive strength in
41 configurations with aluminium skin and linen, where the knockdown factor is less than 10% [15].

42 However, a previous study simulated impact on wood based materials with a damage law available in
43 LS-Dyna [21]. This study showed a deficiency of this type of approach. Additionally, based on their
44 experience of the impact on composite structures [22]–[25] the authors believe that the use of the so-
45 called Discrete Ply Model [23]–[25] modeling strategy would be relevant to model the fracture

46 scenarios of plywood-based structures, in both static and dynamic situations. This strategy is based on
47 only 13 parameters, including energy fracture toughness at interfaces, which should be identified
48 specifically for wood applications.

49 To characterize the glue joint, the standard NF EN 302 (AFNOR 2017) or the former standard DIN
50 53253 (DIN 1964) propose to test the shear strength of the glue joint via longitudinal tensile tests.
51 However, during this type of test, only the strength of the glue line is characterized [26]. Thus,
52 synthetic composite materials standard ASTM D5528 (ASTM 2010) is considered to characterize the
53 toughness of a glued interface in mode I. This opening mode is studied as a priority because, in
54 general among the three modes of propagation of a crack, it is the one that requires the least energy
55 and is therefore the most dangerous for the structure. The mode I toughness of the LVL is generally
56 characterized by a DCB (Double Cantilever Beam) test. This test makes it possible to obtain the
57 Resistance curve of the characterized interface, also called the R-curve. This curve represents the
58 amount of energy required to propagate an initial crack in the interface to be characterized [27]. The
59 few authors who have shown interest in DCB tests on glued wood interfaces, either for LVL or
60 plywood include El Moustaphaoui et al. [28], [29], who characterized the toughness of a 9-ply ceiba
61 plywood interface, without specifying its stacking sequence, using urea-formaldehyde glue. They
62 obtained a G_{Ic} value between 140 J/m² and 200 J/m². Baba et al. [30] were interested in the
63 delamination of beech plywood with a 0°/0° interface and the stacking sequence [0°/90°/0°]_s. They
64 obtained a G_{Ic} value of the order of 20 J/m². This value, which is low compared to that of El
65 Moustaphaoui, can be explained by the addition of rye flour in the urea-formaldehyde glue used to
66 make the test tubes. Other authors have been interested in glued wood interfaces in glulam [31]–[37].
67 The order of magnitude of G_{Ic} values obtained by these studies is a few hundred Joules per square
68 meters.

69 Previous studies only considered 0°/0° delamination interfaces [28]–[37] but, in the case of laminates
70 such as plywood, delamination occurs mainly at 0°/90° interfaces because interlaminar shear is
71 maximum for perpendicularly oriented interfaces. This phenomenon is well known in the field of
72 composites [38] but not studied for wood.

73 In the case of laminates made of synthetic composite materials, the configuration with a 0°/0° interface
74 makes it possible to find a lower bound for the value of G_{Ic} by limiting fiber bridging while keeping
75 the crack in the interface between the 0°/0° plies. The configuration with a 0°/90° interface is more
76 likely to create migration of the crack into the 90° ply and therefore will tend to overestimate the G_{Ic}
77 [39], [40].

78 Moreover, in the case of LVL or plywood, only El Moustaphaoui et al. have computed R-curves [28].
79 Baba et al. have reproduced an R-curve characterizing the G_{Ic} of initiation for various initial cracks
80 [30]. However, once the R-curve is obtained, few physical justifications are provided to explain its
81 evolution and analyze these specimens' fracture surfaces.

82 Therefore, the study presented here aims to provide mode I delamination R-curves for two different
83 interfaces: a 0°/0° interface and a 0°/90° interface. The evolution of the R-curve will be analyzed for
84 Koster poplar (*Populus*) plywood and a comparison will be made between the two interfaces studied.
85 The corresponding fracture toughness will be calculated and analyzed.

86 2. Materials and Experimental Procedures

87 The Double Cantilever Beam (DCB) test consists of applying a load to the ends of the specimen,
88 which causes the crack to propagate in pure mode I. The specimen is placed with an initial crack
89 length (a_0). Figure 1 shows the DCB test and the depiction of the initial crack. The fracture energy can
90 be evaluated using the force-displacement curve (P- δ curve), the crack length (a), and the Irwin-Kies
91 equation [41] (Equation 1):

$$92 \quad G_{Ic} = \frac{P^2}{2b} \frac{dC}{da}$$

93 **Equation 1**

94 with b as the width of the specimen and C as the compliance of the specimen (Equation 2).

$$95 \quad C = \frac{\delta}{P}$$

96 **Equation 2**

97 2.1. Materials and Manufacturing

98 One-millimeter Koster wood veneers were used in the manufacture of the DCB test specimens. The
99 veneer, supplied by the LaBoMaP laboratory in Cluny, France, was produced using a rotary wood
100 peeling machine. The moisture content of the wood was measured at 10.1% with a Relative Standard
101 Deviation (RSD) of 0.4%. The veneers were then stacked and pressed for 5 hours at 10 bars and 25°C.
102 The wood glue used to make the plywood was Kleiberit PUR 510 FIBERBOND, a one-component
103 polyurethane-based glue that hardens by reaction with moisture. The amount of glue used was 250
104 g/m². The density of Koster veneers was 348 kg/m³ (RSD: 4%).

105 Two specimen configurations were made for this study and are illustrated in Figure 2:

- 106 • 8-ply laminates with a $[0^\circ]_8$ stacking sequence to study the $0^\circ/0^\circ$ interface, referred to as “ $0^\circ/0^\circ$
107 specimens”.
- 108 • 9-ply laminates with a $[0^\circ_4, 90^\circ, 0^\circ_4]$ stacking sequence to study the $0^\circ/90^\circ$ interface, referred to
109 as “ $0^\circ/90^\circ$ specimens”. A view of the thickness is shown in Figure 3.

110 Two reference frames will be used to describe the systems (Figure 3):

- 111 • A global reference frame (X,Y,Z) with X oriented along the length of the DCB specimen, Y in
112 its depth, and Z in its thickness (Figure 1).
- 113 • A local reference frame (L,T,R), describing the main directions of the wood, is used to
114 characterize the veneers (L oriented in the direction of the wood fibers (the wood cells), R
115 oriented in the direction of the growth rings, and so in the thickness of the veneers, and T in the
116 transverse direction in the plane of the veneers).

117 It is important to note that, during the manufacture of veneers, lathe checks are created on one of their
118 faces [42], [43]. Lathe checks are small cracks (~0.1mm in the veneer used for this study) that occur
119 along the length of the veneer layers in plywood (Figure 4). These cracks happen when the veneer is
120 manufactured (Figure 5). In addition, the thickness of a wood veneer can be composed of earlywood
121 (wood formed at the beginning of the growing season) and latewood (wood formed later in the
122 season) [44] (Figure 5). It is important to note that the anatomy and the mechanical properties of those
123 two kinds of wood are different [45]–[47].

124 Moreover, unlike carbon composite materials, in wood, and so veneers, not all wood fibers are
125 perfectly aligned, they may have an in-plane and an out-of-plane angle. This is due to the wood nature
126 and, for veneers, the manufacturing process. Since the out-of-plane angle is mainly due to the
127 irregularity of the wood log, when the veneer is peeled, the fibers in the LR plane of the veneer are not
128 aligned with the L direction (Figure 6).

129 The plywood manufactured for the DCB specimen considers the positions of the lathe checks present
130 in the Koster veneer. During stacking, faces with lathe checks are placed on healthy faces, except for
131 the outer plies, where the cracked faces face the inside of the plywood. This stack is called “tight side
132 out and loose side in” and it is this setup that is used in industry for the manufacture of plywood [48].
133 Figure 7 illustrates the stack used for $0^\circ/0^\circ$ specimens.

134 For the $0^\circ/90^\circ$ interfacial orientation, it was therefore decided to orient the cracked face of the 0° ply
135 towards the inside of the interface. Figure 8 illustrates the location of the lathe checks at the $0^\circ/90^\circ$
136 interface in the XZ and YZ planes.

137 A total of 12 specimens per configuration were laser cut. DCB specimens had nominal dimensions of
138 $250(l)\times 25(b)\times 8(h)$ mm³ for the $0^\circ/0^\circ$ series and $250(l)\times 25(b)\times 9(h)$ mm³ for the $0^\circ/90^\circ$ series (shown in
139 Figure 9). Attachment blocks were chosen to attach the DCB specimens to the tension machine. The
140 initial notch (a_0) was made in two stages: a Teflon film was placed during the production of the
141 plywood (as recommended by ASTM D5528 (ASTM 2010)), and then the crack was initiated using a
142 thin cutter blade. The insertion of the cutter blade made it possible to spread the arms slightly so that
143 cracking was initiated without damaging the crack tip. The initiation made with the cutter reduced the
144 variability related to a possible glue cluster at the end of the Teflon film.

145 **2.2. Experimental Setup**

146 DCB tests were performed at ambient temperature and humidity (23.5°C (SD: 0.5°C) and 47% H (SD:
147 2% H)). An Instron 5900 machine was used to perform the tests using a displacement control (Figure
148 10). A 50 kN force cell was installed, with a measurement accuracy of 0.5 N, and the travel speed was
149 set at 20 mm/min.

150 Digital Image Correlation (DIC) was used to track sample deformation. A 5 MP camera (2452x2052
151 pixels) was used to acquire images of the specimens during the test. An infrared thermography (IRT)
152 camera (M3K - Telops) was placed on the other side of the specimens to examine the propagation of
153 damage during the test. The specimens were painted with matt black paint on one side for the IRT
154 camera, to have a constant and maximum emissivity, and with speckles on the other side for image
155 correlation (Figure 10). The speckles were made using spray paint and the size of the patterns was
156 determined according to the experimental configuration to obtain a minimum size of 3 pixels for each
157 speckle [49].

158 A data acquisition system was used to record both the applied load (P) and the vertical displacement of
159 the clamps (δ) (Figure 1), with the acquisition frequency related to image correlation set at 1 Hz.

160 Image correlation data were analyzed with VIC 2D® correlation software. Calibration was carried out
161 using a calibration pattern. The acquisition frequency of the thermal imaging camera was set at 50 Hz.

162 **2.3. Methodology**

163 To compute the fracture energy with a DCB test and the methods presented in ASTM D5528 (ASTM
164 2010), it is necessary to establish a link between compliance C and crack length to obtain dC/da
165 (Equation 1). Many models are documented in the literature, the main ones being:

- 166 • Compliance Calibration (CC) ($C = \lambda_0 a^{\lambda_1}$; λ_0 and λ_1 are constants that need to be identified),
167 described in ISO 15024 (ISO 2001) and ASTM D5528 (ASTM 2010),
- 168 • Modified Compliance Calibration (MCC) ($C^{1/3} = \lambda_1 a/h + \lambda_0$; λ_0 and λ_1 are constants that need to
169 be identified), described in ASTM D5528 (ASTM 2010),
- 170 • Modified Beam Theory (MBT) ($C = 2a^3/3E_1I$) described in ISO 15024 (ISO 2001) and ASTM
171 D5528 (ASTM 2010).

172 DIC was used to obtain the crack length required in the three methods employed in this paper. To
173 post-process DIC images, the size of the subset was fixed so that the subset contained 3 to 4 speckles.

174 The confidence interval of the correlation (called "Sigma") was used to visualize the correlation
175 mismatch and thus estimate the position of the crack tip of the specimens (Figure 11). The Sigma cut-

176 off value chosen was 0.015, which corresponds to the maximum value obtained when calculating the
177 confidence interval between two identical images. The value obtained corresponded to the noise in the
178 study area, so values below 0.015 will not be considered hereafter and are, therefore, not related to the
179 presence of a crack. In addition, the resolution of the camera was 4.55 pixels for 1 mm; so, a
180 correlation confidence interval of 0.015 pixels corresponds to an interval of 0.0033 mm.

181 A Python script was used to track the crack tip using Sigma visualization obtained for each specimen
182 over time. Manual point-by-point monitoring was carried out to obtain the coordinates in millimeters
183 of the tip of the crack at each time.

184 When setting up DIC cameras, a compromise was used to see as many of the samples as possible
185 while keeping a resolution high enough to allow sufficient resolution of the speckles. Therefore, the
186 ends of the specimens were not visible during the test. That is why to obtain the crack length, it is
187 necessary to compute it by using the origin of the crack and consider the bending of the lower arm of
188 all the specimens during the tensile test. For each image captured, three points were tracked and used
189 for specimen curvature interpolation. The first point corresponded to the crack tip (x_f, y_f) , the second
190 to the origin of the crack (x_0, y_0) , and the third was taken on the interface of the specimen between the
191 first and second points (x_1, y_1) , (Figure 12). A second-order function was used to fit this set of points
192 (named $f(x)$). Then, the length of the crack was calculated between the origin of the crack and the
193 crack tip with Equation 3 for each image:

$$194 \quad \mathbf{a} = \int_{x_0}^{x_f} \sqrt{1 + f'(x)^2} dx$$

195 **Equation 3**

196 To validate the method implemented, the measured and calculated lengths of the initial crack were
197 compared for each specimen. Figure 13 illustrates the difference between these two values for all DCB
198 specimens. The average deviation of this difference is 0.33 mm. The accuracy of ½ mm recommended
199 by the ASTM D5528 standard (ASTM 2010) was thus respected.

200 **3. Results**

201 Once the tests were completed, each specimen was inspected to remove specimens with "abnormal"
202 fracture patterns from the study. For example, in some $0^\circ/0^\circ$ series specimens, the crack migrated into
203 the plies at the beginning of the test even though it was initially at the interface. Since the force
204 applied was no longer symmetrical, the crack propagation was no longer in pure mode I and these
205 DCB tests were, therefore, no longer considered valid. For this reason, four specimens were excluded
206 from this study. This migration of the crack in the $0^\circ/0^\circ$ configuration can be explained by the out-of-
207 the-plane variation of the grain angle in the veneers (Figure 14 and Figure 15), not all wood fibers are
208 horizontal and they may have an out-of-plane angle. This phenomenon is not common in DCB tests of
209 composite composites [50]. In addition, as explained in §2.3, the end of the specimen was not visible,
210 and monitoring the crack-tips coordinates (x_f, y_f) was no longer possible for the last propagations and
211 the final fracture, so the last crack propagation leading to the final rupture of the specimen was not
212 considered in this study.

213 The P- δ curves obtained during the tests, keeping only viable specimens, are shown by series in Figure
214 16. On the $0^\circ/90^\circ$ specimens, no anomaly is found during the tests, all the specimens can be used.
215 There is already a greater variability for the $0^\circ/0^\circ$ series compared to the $0^\circ/90^\circ$ series.

216 **3.1. R-curves**

217 For the sake of clarity, only the fracture toughness and R-curves computed with the MCC method will
218 be presented and illustrated in this sub-section.

219 A criterion for estimating repeatability during a DCB test campaign was the variability of the
220 interpolation coefficients determined to correlate compliance and crack length. It is recalled that the
221 MCC method uses an interpolation of $\log(C)$ with $\log(a)$. The fitted curves are shown in Figure 17.
222 The $0^\circ/90^\circ$ series has a lower regression curve slope variability compared to $0^\circ/0^\circ$ series. This lower
223 variability is consistent with the variability observed on the P- δ curves (Figure 16). Note that the
224 average R2 obtained for all fitting curves is 0.988 (SD: 0.011).

225 The first part of crack propagation, corresponding to the initiation of delamination, i.e. first G_{Ic} values,
226 were not considered in this study, in accordance with ASTM D5528 (ASTM 2010). G_{Ic} values were

227 calculated only once the measured force had reached its maximum value and then decreased by 5%.

228 The R-curves obtained by the MCC method are shown in Figure 18.

229 The values for all the test specimens reported in Figure 18 shows that the average value of G_{Ic} is

230 higher for the $0^\circ/0^\circ$ specimens than for the $0^\circ/90^\circ$ ones. This difference is related to the difference of

231 the amount of fiber-bridging. $0^\circ/0^\circ$ specimens exhibited larger amount of fiber-bridging than $0^\circ/90^\circ$

232 ones. To validate this observation, the IR images obtained during the tests were subtracted one by one

233 to obtain the heating between each image. It was thus understood that the heating observed did not

234 come from the background, but from a self-heating in the specimen, related to a dissipation of energy

235 (fiber failure - Figure 19). The IR imagery provides a visualization of irreversible energy dissipation

236 through temperature variations. This self-heating, of the order of 1°C confirmed the presence of fiber

237 rupture, which can be observed in the post-mortem specimens of Figure 19. This variation of energy

238 is associated with fiber rupture because it is a phenomenon more energetic than decohesion alone [51],

239 and it was not throughout the whole test. Fiber bridging is more common in wood than in conventional

240 composites because the variability in the out-of-plane angle of the fibers is much higher than that

241 encountered in carbon composites [52].

242 In addition, there is a tendency for $0^\circ/0^\circ$ ply G_{Ic} to increase throughout propagation. This has however

243 only been observed on a single specimen. The authors believe that this phenomenon cannot be clearly

244 identified in the others because the valid crack propagation (without ply failure or crack migration) is

245 too small. Fiber bridging is a two-step phenomenon: first fibers are being slowly pulled out and then

246 they are broken. That increase in force needed to break the fibers is the reason for the increase in

247 computed G_{Ic} . For the other specimens only the first part of the fiber bridging (fiber pull-out) is

248 observed. It has to be noted that for DCB tests on solid wood, during the fiber bridging, there are as

249 many fibers that break as fibers that bridge in the LT plane [53]. Fiber bridging is therefore a lot more

250 constant throughout crack propagation. In the present study, it seems that the low stiffness of the arms

251 of the DCB specimens made the pulled-out fibers break later.

252 As for the $0^\circ/90^\circ$ series, the G_{Ic} remains quasi-constant, slightly decreasing, when the crack

253 propagates in the specimen. This can be explained by the fact that a lot less fiber bridging occurs in the

254 0°/90° specimens. There was therefore a much greater variability in the 0°/0° specimens. The average
255 values of fracture toughness obtained were: $G_{Ic-0°/0°} = 422 \text{ J/m}^2$ (RSD: 30%) and $G_{Ic-0°/90°} = 247 \text{ J/m}^2$
256 (RSD: 21%). However, once the measured force reaches its maximum value and then decreases by
257 5%, the average initial G_{Ic} , as defined in ASTM D5528 (ASTM 2010), is similar between the 0°/0°
258 specimens and the 0°/90° specimens.

259 To ensure that the potential error from the method used here to track the crack did not have a
260 significant effect on the calculated G_{Ic} values, the G_{Ic} curves obtained were compared with curves
261 obtained by adding artificial random noise on the measured crack lengths. By adding a random
262 measurement error of +/-1.5 mm (a value higher than the maximum error observed in Figure 13), a
263 maximum deviation of 1.75% was measured between the G_{Ic} curves (Figure 20). The method used to
264 calculate G_{Ic} seems to be robust and the potential deviations of the crack length measurements do not
265 disturb the calculated values.

266 In this sub-section, only the MCC method has been used to compute G_{Ic} . However, the results
267 obtained with the two other methods presented (CC and MBT) differed with some specimens. Another
268 method based on beam theory that does not require the use of the crack length can also be used to
269 compute G_{Ic} with Equation 4 [54]:

$$G_{Ic} = \frac{3\delta P}{2b} \times \left(\frac{2}{E_1 I C} \right)^{1/3}$$

271 **Equation 4**

272 The four methods were compared for each specimen. Figure 21 illustrates the relative deviation
273 between the MCC method and the other three methods. The comparison between the 4 methods on the
274 0°/0° specimens shows large differences in half of the specimens. On 0°/90° specimens, there are
275 significant differences only on a small number of specimens. However, there is little difference
276 between the CC and MCC methods, and similarly between the MBT and beam theory methods. The
277 small difference between the MBT method and the beam theory method is reassuring regarding crack
278 tracking. The differences between on one side the methods based on beam theory (MBT and beam
279 theory method) and on the other side the CC and MCC methods can be explained by the presence of

280 fiber bridging for the $0^\circ/0^\circ$ specimens and the presence of fiber bridging in the 90° ply for the $0^\circ/90^\circ$
281 specimens. Methods based on beam theory considered perfect beams without the presence of fiber
282 bridging, on the other hand, CC and MCC methods are calibrated with compliance as a function of the
283 crack length, and so, offer more flexibility and indirectly consider the effect of fiber bridging.

284 However, the relative deviation between the mean G_{Ic} for the $0^\circ/90^\circ$ specimens, computed with the
285 MCC method and the MBT method, differed by only 7.5%. This relative deviation is comparable to
286 that obtained by El Moustaphaoui et al. in Ceiba plywood [29]. Also, for the $0^\circ/0^\circ$ specimens, this
287 relative deviation is 21%. The rest of this paper will use the MCC method, as it, with the CC method,
288 is the one that needs the weakest assumptions about the relationship between compliance and crack
289 length. Furthermore, this method provides R2 coefficients closer to 1 on the calibration curves than the
290 CC method does (Figure 17).

291 **3.2. Fracture Surfaces**

292 In the second step, the fracture surfaces of the specimens were analyzed to highlight the path of the
293 crack and the presence of different physical phenomena. Note that the crack never seemed to
294 propagate in the glue. The break was either adhesive, between the wood and the glue, or cohesive in
295 the wood, but no cohesive break in the glue was observed when the fracture surfaces were observed
296 under a microscope. This phenomenon has already been reported in wood assemblies, where the glue
297 joint is known to be stronger than wood [55]. To relate the crack propagation and the G_{Ic} values
298 obtained, other phenomena have been identified to classify crack propagation:

299 For $0^\circ/0^\circ$ specimens:

- 300 • Crack at the $0^\circ/0^\circ$ interface. It would seem that this crack is cohesive in the wood close to the
301 glue interface between the two plies at 0° , and sometimes adhesive between the wood and the
302 glue. However, these two rupture modes could be observed in the width of the specimen, so
303 they will be considered together for the $0^\circ/0^\circ$ interface crack propagation (zone **2** in Figure 24)
- 304 • Crack migration out of a plane (zone **3** in Figure 24)

305 For $0^\circ/90^\circ$ specimens:

- 306 • Crack at the $0^\circ/90^\circ$ interface (zone **4** in Figure 23)
- 307 • Propagation in the 90° ply (Figure 22 and zone **2** in Figure 23)
- 308 • Crack migration out of a plane or mixed event (zones 3 and 5 in Figure 23, and 3 in Figure 24)

309 As the propagation of the crack in the 90° ply seems to be in the lower part of the ply, the hypothesis
310 that can be advanced for this phenomenon is that the upper part (which includes lathe checks) would
311 not allow a simple propagation of the crack because the lathe check would be filled with glue. The
312 crack would then naturally propagate in the lower part of the ply, which offers the least resistance.

313 In section **3.1**, an average R-curve was plotted for all the specimens. The idea now is to distinguish the
314 different propagation phenomena on each specimen. For example, with specimen $0^\circ/90^\circ$ no. 4, G_{Ic}
315 values are computed from line **1** in Figure 23, according to ASTM D5528 (ASTM 2010). The crack
316 then propagates in the 90° ply (zone **2** in Figure 23) and passes to the interface by tearing fibers (zone
317 **3** in Figure 23). This zone (**3**) is not used for the calculation of the G_{Ic} because it corresponds to a
318 mixed phenomenon (bridging of fibers and passage of the crack at the $0^\circ/90^\circ$ interface). To obtain an
319 average value of G_{Ic} per type of crack propagation according to the classification proposed above,
320 mixed phenomena are not considered since, in mixed zones, the effects of the individual phenomena
321 on the G_{Ic} cannot be distinguished. The crack then propagates to the interface between the 0° and 90°
322 plies (zone **4** in Figure 23). The last part, in purple, corresponds to a similar propagation to zone 3,
323 which cannot be classified and therefore is not considered (zone **5** in Figure 23). The end of the
324 specimen is no longer in the field of view of the cameras and crack tracking is no longer possible (after
325 zone **5** in Figure 23).

326 A similar analysis was carried out on the $0^\circ/0^\circ$ specimens, as illustrated by the example of specimen
327 no. 1 in Figure 24. The difference here is that only the propagation at the $0^\circ/0^\circ$ interface (zone **2** in
328 Figure 24) and particular events (mainly out-of-plane crack migration for these specimens) were
329 considered (zone **3** in Figure 24).

330 By performing this analysis on each specimen, it is possible to calculate the crack propagation energy
331 for each previously distinguished area. For the $0^\circ/0^\circ$ specimens, the value calculated is identical to the

332 mean value obtained in §3.1 (the abnormal values have already been removed from this study as
 333 explained in §3.1), $G_{Ic-0°/0°} = 422 \text{ J/m}^2$ (RSD: 30%). For $90°/0°$ specimens, the study of the fracture
 334 surfaces reveals different R-curves and different average values depending on the zone of propagation
 335 of the crack. To understand the different physical phenomena involved, it is interesting to compare the
 336 present results with a theoretical model based on the Euler-Bernoulli beam theory [56]. This model
 337 provides the following relations (Equation 5 and Equation 6):

$$C = \frac{2a^3}{3E_1I}$$

338
339 **Equation 5**

$$P(\delta) = \sqrt{\frac{2b^2}{3\delta} \sqrt{\frac{G_{Ic}^3 E_1 (h/2)^3}{12}}} = \frac{1}{\sqrt{\delta}} \left(\frac{4}{9} E_1 I \right)^{\frac{1}{4}} (b G_{Ic})^{\frac{3}{4}}$$

340
341 **Equation 6**

342 with I referring to the moment of inertia of a DCB specimen arm and E_1 the longitudinal Young's
 343 modulus.

344 By plotting $P=f(\delta)$ using the measured δ displacement, it is possible to visualize experimental and
 345 theoretical curves on the same graph. Specimen $0°/90°$ no. 4 is taken as an example here. A
 346 comparison of the theoretical values observed with the R-curve of the same specimen gives the
 347 minimum and maximum values observed (~ 55 and $\sim 448 \text{ J/m}^2$ in this case).

348 The differences between the theoretical and experimental curves can be explained. Initially, the
 349 experimental curve follows the theoretical curve for $G_{Ic} = 188 \text{ J/m}^2$ (before zone 1 in Figure 25). There
 350 is then a quasi-constant force on the $P-\delta$ curve, which means that the energy required for the
 351 propagation of the crack increases (zone 1 in Figure 25): when the crack propagates in the $90°$ ply, it
 352 tends to follow lines of least resistance and create some fiber bridging (zone 2 in Figure 25). Fiber
 353 bridging is not as frequent in the $0°/90°$ specimens as in the $0°/0°$ specimen but it nevertheless exists
 354 and is shown in Figure 26. It should be noted, however, the out-of-plane bridging in the $0°/90°$
 355 specimens seems less marked, given the calculated energies compared to the $0°/0°$ specimens. The

356 subsequent drop in force occurs when the crack migrates in an unstable way at the $0^\circ/90^\circ$ interface
357 after tearing fibers (zone 3 in Figure 25). It is then easier for the crack to propagate at the interface
358 than between the wood cells and the locally accumulated energy dissipates, hence the fall of G_{Ic} . Note
359 that this propagation at the interface takes place over a very short time; the value of G_{Ic} obtained can
360 be influenced by viscosity phenomena due to wood or glue due to the dynamic propagation. The crack
361 then resumes a tortuous path between the wood cells in the 90° ply, which again explains the increase
362 in the value of G_{Ic} , as was the case in zone 2 in Figure 25 (zone 4 in Figure 25).

363 Note that, in the case where the crack propagates at the interface, the measurement points taken during
364 the crack propagation are not considered for the calculation of the average value of G_{Ic} , because it is a
365 dynamic propagation. Only the final and stable point is considered when the crack has stabilized. Due
366 to the unstable propagation of the crack, these values underestimate the G_{Ic} (static value) of the
367 interface. Note that the propagation in the $0^\circ/90^\circ$ interface is observed on only two specimens and only
368 a part of the crack propagation occurs at the interface, in both cases, it is an unstable propagation.
369 Once the fracture propagation phenomenon has been detailed, it is possible to plot the R-curves for
370 crack propagation at the $0^\circ/90^\circ$ interface and in the 90° ply (Figure 27).

371 When the crack propagates in the 90° ply, it moves around the fibers, which contributes to the tortuous
372 appearance of each R-curve. The value obtained for the fracture toughness in the 90° ply is $G_{Ic-90^\circ\text{-ply}} =$
373 247 J/m^2 (RSD: 24%).

374 When the crack moves towards the $0^\circ/90^\circ$ interface, there is a significant decrease in the value of G_{Ic} .
375 This is because the crack no longer needs to bypass or break fibers to propagate and so requires a
376 smaller amount of energy. The average value of the critical energy is obtained by taking the values
377 calculated once the crack is installed in the interface. In the present case, only two values were
378 obtained; they are visible in Figure 27. The value found for the critical fracture toughness at the
379 interface $0^\circ/90^\circ$ is $G_{Ic-0^\circ/90^\circ\text{-interface}} = 62 \text{ J/m}^2$ (RSD: 28%). However, a low degree of confidence is to
380 apply to this value given the very low number of test configurations on which this phenomenon
381 appeared and its dynamic aspect. The value to use is therefore $G_{Ic-90^\circ\text{-ply}} = 247 \text{ J/m}^2$ (RSD: 24%).

382 **4. Discussion**

383 In the literature, the values of G_{Ic} on a $0^\circ/0^\circ$ interface of LVL or glulam are between about 20 and 850
 384 J/m^2 . These values are summarized in Table 1.

Authors	Material	G_{Ic} (J/m ²) Min/max
[30]	6-ply beech plywood [0°/90°/0°]/[0°/90°/0°]	~20
[28]	9-ply ceiba plywood [undisclosed stacking sequence]	~140 to 200
[33]	Beech glulam	~30 to 80
[37]	Poplar glulam	~120 to 230
[31]	Scots pine glulam	~150 to 250
[32]	Poplar glulam	~200 to 300
[34]	Maritime pine glulam	~220 to 465
[35]	Maritime pine glulam	~ 400 to 550
[36]	Beech glulam	~ 827 ± 239

385 **Table 1 – Comparison of the orders of magnitude of G_{Ic}**

386 Few authors have investigated plywood toughness, which is why some G_{Ic} values obtained on glulam
 387 are compared here. It is important to note that the thicknesses of wood lumber and veneers are not
 388 identical and therefore there is a scale effect between these materials. However, the differences
 389 between the authors' findings can be explained mainly by the type of wood and glue used in the
 390 manufacturing of the plywood or glulam characterized. The toughness of a glued assembly is strongly
 391 correlated with the nature of the wood-glue combination. In addition, the fracture energy of the
 392 assembly will also be influenced by the roughness of the wood, the thickness of the glue joint or
 393 Young's modulus of the material characterized [57]. Similarly, a strong dispersion is expected on tests
 394 such as DCB applied to wood and wood composite materials due to the heterogeneity of wood
 395 material and the variability of its mechanical properties [57]. Some average values for standard
 396 composites in aeronautics are summarized in Table 2. The mean value of toughness obtains for $0^\circ/0^\circ$
 397 specimens is in the same order of magnitude as thermoset composites.

Authors	Material	G_{Ic} (J/m ²)
[58]	UD carbon/epoxy 1st generation (type 3506)	60
[39]	UD carbon/epoxy 2nd generation (type M21)	450
[59]	UD carbon/PEEK (type APC-2)	2200
[60]	UD carbon/PPS	1100
[38]	U.D. Glass/epoxy	800
[61]	U.D. Glass-E/polyester	300

398

Table 2 – Some G_{Ic} values for standard composites in aeronautics [62]

399 The literature does not provide a value of G_{Ic} for a $0^\circ/90^\circ$ interface in the case of plywood. However,
400 given the results obtained during this study, it can be seen that the value of G_{Ic} for a $0^\circ/90^\circ$ interface
401 ($G_{Ic-90^\circ} = 247 \text{ J/m}^2$ (RSD: 21%)) is lower than for a $0^\circ/0^\circ$ interface ($G_{Ic-0^\circ/0^\circ} = 422 \text{ J/m}^2$ (RSD: 30%))
402 because fiber bridging is less present than in a $0^\circ/0^\circ$ interface. Note that the value of G_{Ic} for an $0^\circ/0^\circ$
403 interface measured experimentally overestimates the value of delamination compared to a pure
404 interface without the effects of fiber bridging and fiber rupture. It is therefore possible to wonder
405 whether the toughness characterized for a $0^\circ/90^\circ$ interface is not to be preferred if the aim is to obtain
406 a numerical value of the mode I fracture toughness of a plywood interface by limiting the influence of
407 fiber bridging. Moreover, according to research [63], the interface $0^\circ/90^\circ$ is the most susceptible to
408 delamination in cases of impact-induced delamination. The value obtained will be a value that is less
409 influenced by fiber bridging and closer to the theoretical value that will subsequently be used for the
410 implementation of a finite element model to simulate the glued interface.

411 It is also interesting to compare the fracture pattern found in this study with those recorded in DCB
412 tests on carbon fiber composite materials. The configuration with a $0^\circ/0^\circ$ interface allows the
413 boundary value of G_{Ic} to be lowered in the case of synthetic composite materials because it is the
414 configuration that gives the least fiber bridging and the 0° fibers at the interface prevent delamination
415 migration [39], [64], [65]. Figure 28 illustrates a representative side view of the crack path of such an
416 interface.

417 In the case of wood, the crack rapidly migrates outside the initial interface. There are several possible
418 explanations for this phenomenon. First, the wood has fibers with a non-zero out-of-plane deviation of
419 the fiber angle due to the manufacturing process, a situation that is much less common for composites.
420 Additionally, the thickness of a wood veneer can be composed of earlywood and latewood (Figure 5)
421 and this heterogeneity could create an easier propagation path for the crack. Finally, in wood
422 assemblies, the glue joint is known to be stronger than wood [55]. This phenomenon can cause the
423 crack to propagate cohesively near the interface for the $0^\circ/0^\circ$ specimens and mostly in the 90° ply for
424 the $0^\circ/90^\circ$ specimens. This is exactly what has been observed on IMA/M21E composites: the glued
425 interface is stronger than the plies [23], [66].

426 In the second configuration of composite materials, with a $0^\circ/90^\circ$ interface, the crack may change
427 plane during delamination [39] (Figure 29). [This delamination migration in synthetic composite](#)
428 [material tends to increase the fracture area and to dissipate more energy \[40\]. According to Sebaey et](#)
429 [al., their numerical model demonstrates that as the bending stiffness of specimen arms decreases, there](#)
430 [is an increased propensity for delamination migration at the interface \[67\]. However, for plywood,](#)
431 [delamination migration doesn't occur on specimen with \$0^\circ/90^\circ\$ interface.](#)

432 [Concerning fiber bridging, the phenomenon is less important for this configuration compared to](#)
433 [specimens with \$0^\circ/0^\circ\$ interface. Due to the propagation of the crack in the \$90^\circ\$ ply, the few fiber](#)
434 [bridging behavior observed is comparable to that of a \$90^\circ/90^\circ\$ interface in synthetic composite \[40\],](#)
435 [\[65\].](#)

436 Considering the nature of the wood, with the presence of out-of-plane fibers and a greater fiber
437 bridging, it is possible to explain why the value of G_{Ic} for a $0^\circ/0^\circ$ interface is not a lower bound G_{Ic}
438 value for plywood while this is the case for composite materials [39], [40], [50]. In addition, fracture
439 pattern and crack propagation appear similar when crack propagations are compared for $0^\circ/90^\circ$
440 interfaces in the cases of plywood and composite materials.

441 **5. Conclusions and Perspectives**

442 The effects of interfacial orientation for two different configurations were investigated in DCB tests on
443 poplar plywood. The following conclusions can be drawn from the results of the study:

- 444 • On the R-curves, $G_{Ic-0^\circ/0^\circ}$ tends to increase, due to fiber bridging, while the average value of
445 $G_{Ic-0^\circ/90^\circ}$ remains quasi-constant, slightly decreasing, as a function of the crack propagation.
- 446 • The values of $G_{Ic-0^\circ/0^\circ}$ ($G_{Ic-0^\circ/0^\circ} = 422 \text{ J/m}^2$ (RSD: 30%)) are more scattered than $G_{Ic-0^\circ/90^\circ}$ (G_{Ic-}
447 $0^\circ/90^\circ = 247 \text{ J/m}^2$ (RSD: 21%)). This is explained by the presence of fiber bridging during the
448 crack propagation in the case of the $0^\circ/0^\circ$ interface.
- 449 • On average, the $G_{Ic-0^\circ/0^\circ}$ has a higher value than $G_{Ic-0^\circ/90^\circ}$, due to the presence of fiber bridging.
450 It is interesting to perform DCB tests with a $0^\circ/90^\circ$ interface to obtain G_{Ic} values for plywood,
451 for the development of numerical models. This interface corresponds to those most likely to
452 delaminate. The apparent toughness, i.e. the toughness computed with the influence of
453 structural effects such as fiber bridging, could differ from the intrinsic material toughness
454 value. However, the values presented in this article provide values for comparing the effect of
455 the interface on delamination. It should also be noted that some fiber bridging also influences
456 the values obtained on $0^\circ/90^\circ$ specimens.

457 To implement a numerical model of wood-based composite, specimen characterization with $0^\circ/90^\circ$
458 interfaces seems to provide a lower bound for the interface toughness value that could serve as a
459 reference for modelling glued interfaces of plywood or LVL, for example. However, further research
460 is needed to determine the influence of new interface orientations on these toughness values and to
461 identify the influence of this interface on the measured values. In addition, in low-velocity impact
462 failure, mode I initiate the delamination in composite laminates, but then mode II (plane shear) is
463 predominant in the propagation of the crack due to high shear stress at the interface [68]. To set up a
464 digital model of plywood, it would then be necessary to characterize mode II toughness through, for
465 example, ENF (End Notched Flexure) tests. [However, it has to be underlined that delamination
466 migration can also occur in mode II propagation, it's already observed in LVL \[69\] and in carbon fibre
467 composite with ENF tests \[70\], \[71\].](#)

468 6. Acknowledgments

469 The research that led to the results presented above received funds from the French National Research
470 Agency under the BOOST project (ANR-21-CE43-0008-01). The authors thank the LaBoMaP
471 Laboratory, Cluny, France for providing the Poplar veneers used in this study, through the research
472 project ANR BOOST.

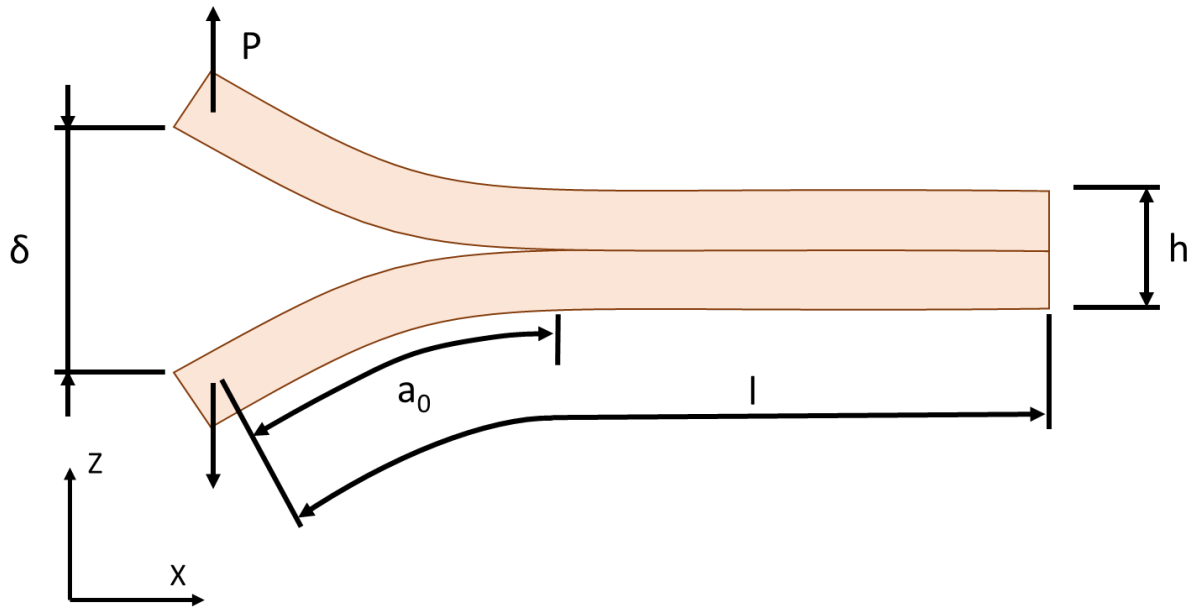
473 7. References

- 474 [1] G. Wimmers, ‘Wood: a construction material for tall buildings’, *Nat. Rev. Mater.*, vol. 2, p.
475 17051, Jul. 2017, doi: 10.1038/natrevmats.2017.51.
- 476 [2] J. Ye and C. Fivet, ‘The zaojing: review of a unique wooden construction typology’, *Int. J.*
477 *Constr. Hist. Soc.*, vol. 35, no. 1, pp. 22–49, Jun. 2020, doi: 10.5281/zenodo.3941502.
- 478 [3] B. Castanie, C. Bouvet, and M. Ginot, ‘Review of composite sandwich structure in aeronautic
479 applications’, *Compos. Part C Open Access*, vol. 1, p. 100004, Aug. 2020, doi:
480 10.1016/j.jcomc.2020.100004.
- 481 [4] G. Jungmeier, F. Werner, A. Jarnehammar, C. Hohenthal, and K. Richter, ‘Allocation in LCA of
482 wood-based products experiences of cost action E9: Part I. Methodology’, *Int. J. Life Cycle*
483 *Assess.*, vol. 7, no. 5, pp. 290–294, Sep. 2002, doi: 10.1007/BF02978890.
- 484 [5] G. Jungmeier, F. Werner, A. Jarnehammar, C. Hohenthal, and K. Richter, ‘Allocation in LCA of
485 wood-based products experiences of cost action E9: Part II. Examples’, *Int. J. Life Cycle Assess.*,
486 vol. 7, no. 6, pp. 369–375, Nov. 2002, doi: 10.1007/BF02978686.
- 487 [6] R. Bergman, M. Puettmann, A. Taylor, and K. E. Skog, ‘The Carbon Impacts of Wood
488 Products’, *For. Prod. J.*, vol. 64, no. 7–8, pp. 220–231, Dec. 2014, doi: 10.13073/FPJ-D-14-
489 00047.
- 490 [7] C. Cornillier and E. Vial, ‘L’Analyse de Cycle de Vie (ACV) appliquée aux produits bois : bilan
491 énergétique et prise en compte du carbone biomasse’, presented at the IXème Colloque Sciences
492 et Industrie du Bois, 2008, p. 16.
- 493 [8] K. Tamanna, S. N. Raman, M. Jamil, and R. Hamid, ‘Utilization of wood waste ash in
494 construction technology: A review’, *Constr. Build. Mater.*, vol. 237, p. 117654, Mar. 2020, doi:
495 10.1016/j.conbuildmat.2019.117654.
- 496 [9] Finnish Woodworking Industries Federation, Ed., *LVL handbook Europe*. Helsinki: Federation
497 of the Finnish Woodworking Industries, 2019.
- 498 [10] Y. Kiliç, E. Burdurlu, G. C. Elibol, and M. Ulupinar, ‘Effect of Layer Arrangement on
499 Expansion, Bending Strength and Modulus of Elasticity of Solid Wood and Laminated Veneer
500 Lumber (LVL) Produced from Pine and Poplar’, p. 7, 2010.
- 501 [11] R. H. Leicester and R. C. Bunker, ‘Fracture at butt joints in laminated pine’, *For. Prod J* 192 59-
502 60, 1969.
- 503 [12] H. Sasaki and A. A. Abdullahi, ‘Lumber: Laminated Veneer’, in *Reference Module in Materials*
504 *Science and Materials Engineering*, Elsevier, 2016, p. B9780128035818020000. doi:
505 10.1016/B978-0-12-803581-8.01989-5.
- 506 [13] J. A. Youngquist, T. L. Laufenberg, and B. S. Bryant, ‘End jointing of laminated veneer lumber
507 for structural use’, *For. Prod. J.*, p. 8, 1984.
- 508 [14] R. Guélou, F. Eyma, A. Cantarel, S. Rivallant, and B. Castanié, ‘A comparison of three wood
509 species (poplar, birch and oak) for crash application’, *Eur. J. Wood Wood Prod.*, Aug. 2022, doi:
510 10.1007/s00107-022-01871-x.
- 511 [15] J. Susainathan, F. Eyma, E. De Luycker, A. Cantarel, C. Bouvet, and B. Castanie, ‘Experimental
512 investigation of compression and compression after impact of wood-based sandwich structures’,
513 *Compos. Struct.*, vol. 220, pp. 236–249, Jul. 2019, doi: 10.1016/j.compstruct.2019.03.095.
- 514 [16] R. Guélou, F. Eyma, A. Cantarel, S. Rivallant, and B. Castanié, ‘Static crushing of wood based
515 sandwich composite tubes’, *Compos. Struct.*, vol. 273, 2021, doi:
516 10.1016/j.compstruct.2021.114317.

- 517 [17] R. Guélou, F. Eyma, A. Cantarel, S. Rivallant, and B. Castanié, ‘Crashworthiness of poplar
518 wood veneer tubes’, *Int. J. Impact Eng.*, vol. 147, p. 103738, Jan. 2021, doi:
519 10.1016/j.ijimpeng.2020.103738.
- 520 [18] R. Guélou, F. Eyma, A. Cantarel, S. Rivallant, and B. Castanié, ‘Dynamic crushing of wood-
521 based sandwich composite tubes’, *Mech. Adv. Mater. Struct.*, pp. 1–21, Oct. 2021, doi:
522 10.1080/15376494.2021.1991533.
- 523 [19] J. Susainathan, F. Eyma, E. De Luycker, A. Cantarel, and B. Castanie, ‘Manufacturing and
524 quasi-static bending behavior of wood-based sandwich structures’, *Compos. Struct.*, vol. 182, pp.
525 487–504, Dec. 2017, doi: 10.1016/j.compstruct.2017.09.034.
- 526 [20] J. Susainathan, F. Eyma, E. De Luycker, A. Cantarel, and B. Castanie, ‘Experimental
527 investigation of impact behavior of wood-based sandwich structures’, *Compos. Part Appl. Sci.*
528 *Manuf.*, vol. 109, pp. 10–19, Jun. 2018, doi: 10.1016/j.compositesa.2018.02.029.
- 529 [21] J. Susainathan, F. Eyma, E. De Luycker, A. Cantarel, and B. Castanie, ‘Numerical modeling of
530 impact on wood-based sandwich structures’, *Mech. Adv. Mater. Struct.*, vol. 27, no. 18, Art. no.
531 18, Sep. 2020, doi: 10.1080/15376494.2018.1519619.
- 532 [22] S. Abrate, B. Castanié, and Y. D. S. Rajapakse, Eds., *Dynamic Failure of Composite and*
533 *Sandwich Structures*, vol. 192. in *Solid Mechanics and Its Applications*, vol. 192. Dordrecht:
534 Springer Netherlands, 2013. doi: 10.1007/978-94-007-5329-7.
- 535 [23] L. Adam, C. Bouvet, B. Castanié, A. Daidié, and E. Bonhomme, ‘Discrete ply model of circular
536 pull-through test of fasteners in laminates’, *Compos. Struct.*, vol. 94, no. 10, pp. 3082–3091, Oct.
537 2012, doi: 10.1016/j.compstruct.2012.05.008.
- 538 [24] C. Bouvet, B. Castanié, M. Bizeul, and J.-J. Barrau, ‘Low velocity impact modelling in laminate
539 composite panels with discrete interface elements’, *Int. J. Solids Struct.*, vol. 46, no. 14, pp.
540 2809–2821, Jul. 2009, doi: 10.1016/j.ijsolstr.2009.03.010.
- 541 [25] J. Serra, C. Bouvet, B. Castanié, and C. Petiot, ‘Scaling effect in notched composites: The
542 Discrete Ply Model approach’, *Compos. Struct.*, vol. 148, pp. 127–143, Jul. 2016, doi:
543 10.1016/j.compstruct.2016.03.062.
- 544 [26] J. Konnerth, W. Gindl, M. Harm, and U. Müller, ‘Comparing dry bond strength of spruce and
545 beech wood glued with different adhesives by means of scarf- and lap joint testing method’, *Holz*
546 *Als Roh- Werkst.*, vol. 64, no. 4, pp. 269–271, Aug. 2006, doi: 10.1007/s00107-006-0104-1.
- 547 [27] F. Lachaud, ‘Delamination de matériaux composites a fibres de carbone et a matrices organiques :
548 etude numerique et experimentale, suivi par emission acoustique’, PhD Thesis, Université de
549 Toulouse - ISAE, Toulouse, 1997.
- 550 [28] A. El Moustaphaoui, A. Chouaf, and K. Kimakh, ‘Experimental and numerical study of the
551 delamination of Ceiba plywood under mode I, mode II and mixed-mode (I + II) loading using
552 the DCB, ELS and MMF tests’, *Int. J. Fract.*, Jun. 2021, doi: 10.1007/s10704-021-00557-4.
- 553 [29] A. El Moustaphaoui, A. Chouaf, K. Kimakh, and M. Chergui, ‘Characterization of ceiba
554 plywood delamination in mode I using an energetic criterion’, *Wood Res.*, vol. 64, p. 12, 2019.
- 555 [30] M. N. Baba, F. Dogaru, I. Curtu, G. Dinu, and M. Bayer, ‘Experimental Determination of
556 Interlaminar Fracture Toughness of Wood Laminated Composite Specimens under DCB Test’,
557 *Mater. Plast.*, p. 5, 2010.
- 558 [31] Y. Zhao, Z. Li, and B. Xu, ‘Mixed-mode (I/II) interlaminar fracture of glued-laminated timber’,
559 *Mater. Des.*, vol. 131, pp. 210–218, Oct. 2017, doi: 10.1016/j.matdes.2017.05.070.
- 560 [32] J. Jennings, ‘Investigating the Surface Energy, and Bond Performance of Compression Densified
561 Wood’, Blacksburg, Virginia, 2003.
- 562 [33] M. Rhême, J. Botsis, J. Cugnani, and P. Navi, ‘Influence of the moisture content on the fracture
563 characteristics of welded wood joint. Part 1: Mode I fracture’, *Holzforschung*, vol. 67, no. 7, pp.
564 747–754, 2013.
- 565 [34] J. Xavier, J. Morais, N. Dourado, and M. F. S. F. De Moura, ‘Measurement of Mode I and Mode
566 II Fracture Properties of Wood-Bonded Joints’, *J. Adhes. Sci. Technol.*, vol. 25, no. 20, pp.
567 2881–2895, Jan. 2011, doi: 10.1163/016942411X576563.
- 568 [35] F. G. A. Silva, J. Xavier, F. A. M. Pereira, J. J. L. Morais, N. Dourado, and M. F. S. F. Moura,
569 ‘Determination of cohesive laws in wood bonded joints under mode I loading using the DCB
570 test’, *Holzforschung*, vol. 67, no. 8, Art. no. 8, Dec. 2013, doi: 10.1515/hf-2013-0012.

- 571 [36] S. Myslicki, T. Vallée, O. Bletz-Mühldorfer, F. Diehl, L. C. Lavarec, and R. Créac’Hcadeç,
572 ‘Fracture mechanics based joint capacity prediction of glued-in rods with beech laminated
573 veneer lumber’, *J. Adhes.*, vol. 95, no. 5–7, pp. 405–424, Jun. 2019, doi:
574 10.1080/00218464.2018.1538879.
- 575 [37] C. R. Scoville, ‘Characterizing the Durability of PF and pMDI Adhesive Wood Composites
576 Through Fracture Testing’, PhD Thesis, Virginia Tech, 2001. Accessed: May 09, 2022. [Online].
577 Available: <https://vtechworks.lib.vt.edu/handle/10919/35353>
- 578 [38] D. Gay, *Composite Materials: Design and Applications*, 3rd edition. CRC Press, 2014.
- 579 [39] P. Prombut, ‘Caractérisation de la propagation de délaminage des stratifiées composites
580 multidirectionnelles’, PhD Thesis, Université de Toulouse III – Paul Sabatier, Toulouse, 2007.
- 581 [40] Y. Gong *et al.*, ‘Delamination in carbon fiber epoxy DCB laminates with different stacking
582 sequences: R-curve behavior and bridging traction-separation relation’, *Compos. Struct.*, vol.
583 262, p. 113605, Apr. 2021, doi: 10.1016/j.compstruct.2021.113605.
- 584 [41] G. R. Irwin and J. A. Kies, ‘The welding journal’, *Res Suppl*, vol. 33, p. 193, 1954.
- 585 [42] L. Denaud *et al.*, ‘Influence of Peeling Process Parameters on Veneer Lathe Check Properties’,
586 presented at the 24th International Wood Machining Semina, Corvallis, OR, USA, Aug. 2019.
- 587 [43] G. Pot, L. Denaud, J.-C. Butaud, S. Girardon, R. Collet, and F. Cottin, ‘Experimental study of
588 the influence of veneer lathe checks on LVL elastic mechanical properties’, Aug. 2016.
- 589 [44] S. Stefanowski, R. Frayssinhes, G. Pinkowski, and L. Denaud, ‘Study on the in-process
590 measurements of the surface roughness of Douglas fir green veneers with the use of laser
591 profilometer’, *Eur. J. Wood Wood Prod.*, vol. 78, no. 3, pp. 555–564, May 2020, doi:
592 10.1007/s00107-020-01529-6.
- 593 [45] I. Rahayu, L. Denaud, R. Marchal, and W. Darmawan, ‘Ten new poplar cultivars provide
594 laminated veneer lumber for structural application’, *Ann. For. Sci.*, vol. 72, no. 6, pp. 705–715,
595 Sep. 2015, doi: 10.1007/s13595-014-0422-0.
- 596 [46] J. Gáborik and K. Káčerová, ‘Bending properties of laminated wood from juvenile poplar.’,
597 *Proc. 2nd Int. Sci. Conf. Woodwork. Tech. Zalesina Croat. 11-15 Sept. 2007*, pp. 233–240, 2007.
- 598 [47] F. F. P. Kollmann, W. A. Côté, E. W. Kuenzi, and A. J. Stamm, *Principles of Wood Science and*
599 *Technology: Solid wood*. G. Allen & Unwin, 1968.
- 600 [48] W. Leggate, R. McGavin, and H. Bailleres, *A guide to manufacturing rotary veneer and*
601 *products from small logs*, ACIAR Monograph. 2017.
- 602 [49] P. Reu, ‘All about speckles: Speckle Size Measurement’, *Exp. Tech.*, vol. 38, no. 6, pp. 1–2,
603 Nov. 2014, doi: 10.1111/ext.12110.
- 604 [50] A. Ramji, Y. Xu, M. Yasaei, M. Grasso, and P. Webb, ‘Delamination migration in CFRP
605 laminates under mode I loading’, *Compos. Sci. Technol.*, vol. 190, p. 108067, Apr. 2020, doi:
606 10.1016/j.compscitech.2020.108067.
- 607 [51] T. Lisle, C. Bouvet, N. Hongkarnjanakul, M.-L. Pastor, S. Rivallant, and P. Margueres, ‘Measure
608 of fracture toughness of compressive fiber failure in composite structures using infrared
609 thermography’, *Compos. Sci. Technol.*, vol. 112, pp. 22–33, May 2015, doi:
610 10.1016/j.compscitech.2015.03.005.
- 611 [52] M. Pramreiter, S. C. Bodner, J. Keckes, A. Stadlmann, C. Kumpenza, and U. Müller, ‘Influence
612 of Fiber Deviation on Strength of Thin Birch (*Betula pendula* Roth.) Veneers’, *Materials*, vol.
613 13, no. 7, Art. no. 7, Mar. 2020, doi: 10.3390/ma13071484.
- 614 [53] J. L. Gómez-Royuela, A. Majano-Majano, A. J. Lara-Bocanegra, J. Xavier, and M. F. S. F. de
615 Moura, ‘Evaluation of R-curves and cohesive law in mode I of European beech’, *Theor. Appl.*
616 *Fract. Mech.*, vol. 118, p. 103220, Apr. 2022, doi: 10.1016/j.tafmec.2021.103220.
- 617 [54] S. Hashemi, A. Jame Kinlock, and J. M. Williams, ‘The analysis of interlaminar fracture in
618 uniaxial fibre-polymer composites’, *Proc. R. Soc. Lond. Math. Phys. Sci.*, vol. 427, no. 1872, pp.
619 173–199, Jan. 1990, doi: <https://doi.org/10.1098/rspa.1990.0007>.
- 620 [55] R. J. Ross and F. P. Laboratory. USDA Forest Service., ‘Wood handbook : wood as an
621 engineering material’, U.S. Department of Agriculture, Forest Service, Forest Products
622 Laboratory, Madison, WI, FPL-GTR-190, 2010. doi: 10.2737/FPL-GTR-190.
- 623 [56] N. Ben Salem, ‘Fiabilité des assemblages structuraux collés pour applications spatiales’, PhD
624 Thesis, Bordeaux 1, 2012. Accessed: Oct. 19, 2022. [Online]. Available:
625 <https://www.theses.fr/2012BOR14681>

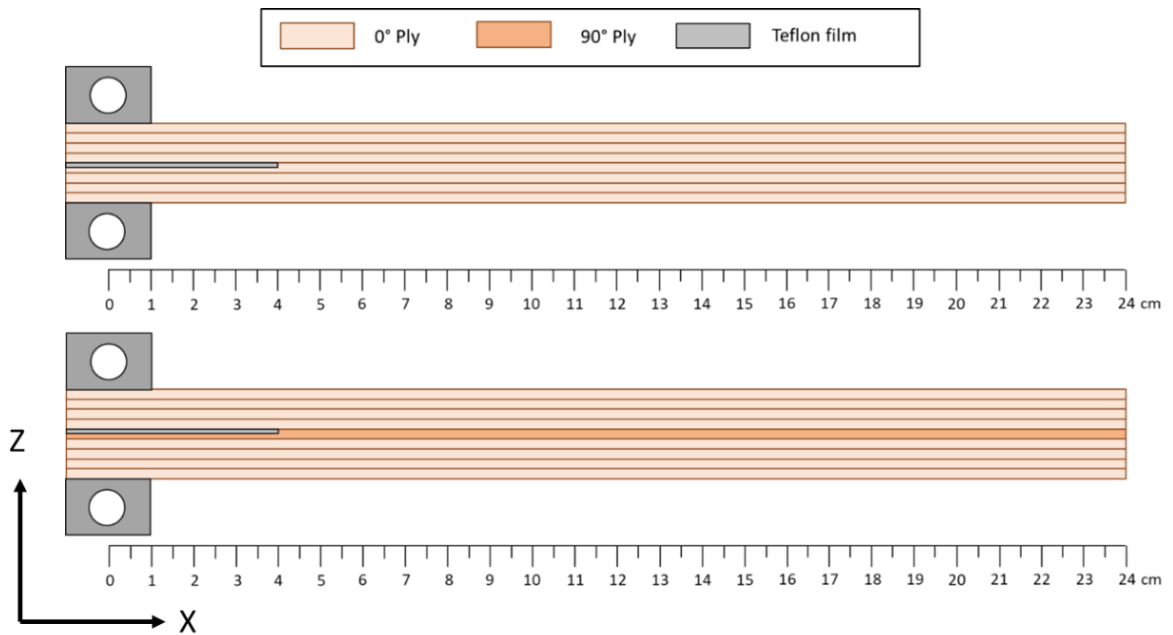
- 626 [57] G. Pluinage, *La rupture du bois et de ses composites*, Cépaduès-Éditions. 1992. Accessed: Aug.
627 24, 2021. [Online]. Available: <https://www.eyrolles.com/BTP/Livre/la-rupture-du-bois-et-de->
628 [ses-composites-9782854282924/](https://www.eyrolles.com/BTP/Livre/la-rupture-du-bois-et-de-ses-composites-9782854282924/)
- 629 [58] B. W. Kim and A. H. Mayer, ‘Influence of fiber direction and mixed-mode ratio on delamination
630 fracture toughness of carbon/epoxy laminates’, *Compos. Sci. Technol.*, vol. 63, no. 5, pp. 695–
631 713, Apr. 2003, doi: 10.1016/S0266-3538(02)00258-0.
- 632 [59] S. Hashemi, A. J. Kinloch, and J. G. Williams, ‘The Effects of Geometry, Rate and Temperature
633 on the Mode I, Mode II and Mixed-Mode I/II Interlaminar Fracture of Carbon-Fibre/Poly(ether-
634 ether ketone) Composites’, *J. Compos. Mater.*, vol. 24, no. 9, pp. 918–956, Sep. 1990, doi:
635 10.1177/002199839002400902.
- 636 [60] F. Sacchetti, W. J. B. Groupe, L. L. Warnet, and I. F. Villegas, ‘Effect of cooling rate on the
637 interlaminar fracture toughness of unidirectional Carbon/PPS laminates’, *Eng. Fract. Mech.*, vol.
638 203, pp. 126–136, Nov. 2018, doi: 10.1016/j.engfracmech.2018.02.022.
- 639 [61] A. Szekrényes, ‘Delamination fracture analysis in the GII–GIII plane using prestressed
640 transparent composite beams’, *Int. J. Solids Struct.*, vol. 44, no. 10, pp. 3359–3378, May 2007,
641 doi: 10.1016/j.ijsolstr.2006.09.029.
- 642 [62] C. Bouvet, ‘Mécanique de la rupture des composites : délaminage et fissuration’, *Systèmes*
643 *Aéronautiques Spatiaux*, Feb. 2019, doi: 10.51257/a-v1-trp4043.
- 644 [63] D. Liu, ‘Impact-Induced Delamination: A View of Bending Stiffness Mismatching’, *J. Compos.*
645 *Mater.*, vol. 22, 1988.
- 646 [64] A. Sohrabi, M. Pourhosseinshahi, and B. Mohammadi, ‘Prediction of mode I fracture behavior
647 of delaminated 0//90 interface in cross-ply laminated composites from the SERR of classical
648 unidirectional DCB specimen’, *Compos. Struct.*, vol. 317, p. 117080, Aug. 2023, doi:
649 10.1016/j.compstruct.2023.117080.
- 650 [65] M. S. Bin Mohamed Rehan, J. Rousseau, S. Fontaine, and X. J. Gong, ‘Experimental study of
651 the influence of ply orientation on DCB mode-I delamination behavior by using multidirectional
652 fully isotropic carbon/epoxy laminates’, *Compos. Struct.*, vol. 161, pp. 1–7, Feb. 2017, doi:
653 10.1016/j.compstruct.2016.11.036.
- 654 [66] S. Chaïbi, ‘Prévision des endommagements induits par un impact basse vitesse/basse énergie au
655 sein de matériaux composites stratifiés carbone-epoxy de dernière génération’, PhD Thesis,
656 Université de Toulouse - ISAE, Toulouse, 2022.
- 657 [67] T. A. Sebaey, N. Blanco, C. S. Lopes, and J. Costa, ‘Numerical investigation to prevent crack
658 jumping in Double Cantilever Beam tests of multidirectional composite laminates’, *Compos. Sci.*
659 *Technol.*, vol. 71, no. 13, pp. 1587–1592, Sep. 2011, doi: 10.1016/j.compscitech.2011.07.002.
- 660 [68] C. Bouvet, S. Rivallant, and J. J. Barrau, ‘Low velocity impact modeling in composite laminates
661 capturing permanent indentation’, *Compos. Sci. Technol.*, vol. 72, no. 16, pp. 1977–1988, Nov.
662 2012, doi: 10.1016/j.compscitech.2012.08.019.
- 663 [69] B. Franke and P. Quenneville, ‘Analysis of the fracture behavior of Radiata Pine timber and
664 Laminated Veneer Lumber’, *Eng. Fract. Mech.*, vol. 116, pp. 1–12, Jan. 2014, doi:
665 10.1016/j.engfracmech.2013.12.004.
- 666 [70] S. Oshima, A. Mamishin, M. Hojo, M. Nishikawa, N. Matsuda, and M. Kanesaki, ‘High-
667 resolution in situ characterization of micromechanisms in CFRP laminates under mode II
668 loading’, *Eng. Fract. Mech.*, vol. 260, p. 108189, Feb. 2022, doi:
669 10.1016/j.engfracmech.2021.108189.
- 670 [71] M. Olave, I. Vara, H. Usabiaga, L. Aretxabaleta, S. V. Lomov, and D. Vandepitte, ‘Nesting
671 effect on the mode II fracture toughness of woven laminates’, *Compos. Part Appl. Sci. Manuf.*,
672 vol. 74, pp. 174–181, Jul. 2015, doi: 10.1016/j.compositesa.2015.03.020.
- 673 [72] N. M. M. Dourado, M. F. S. F. de Moura, J. J. L. Morais, and M. A. L. Silva, ‘Estimate of
674 resistance-curve in wood through the double cantilever beam test’, *Holzforschung*, vol. 64, no. 1,
675 Jan. 2010, doi: 10.1515/hf.2010.010.
- 676 [73] R. Duriot *et al.*, ‘New Perspectives for LVL Manufacturing from Wood of Heterogeneous
677 Quality—Part. 1: Veneer Mechanical Grading Based on Online Local Wood Fiber Orientation
678 Measurement’, *Forests*, vol. 12, no. 9, Art. no. 9, Sep. 2021, doi: 10.3390/f12091264.
- 679 [74] H. G. Richter, K. Gembruch, and G. Koch, ‘CITESwoodID - introduction’, *delta-intkey*, Sep. 20,
680 2019. <https://www.delta-intkey.com/citeswood/en/intro.htm> (accessed Jan. 13, 2023).



682

683

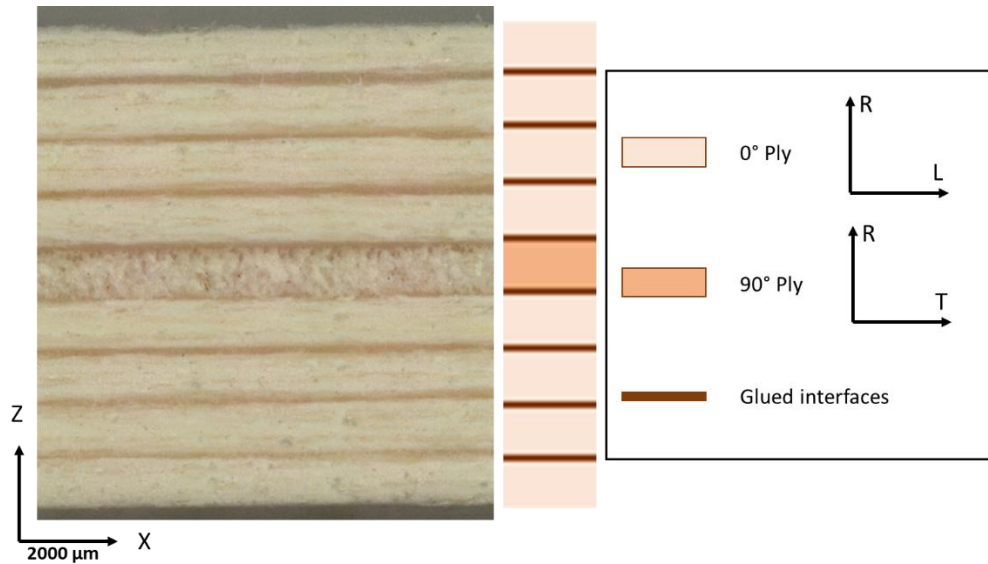
Figure 1- Sketch of the double cantilever beam [72]



684

685

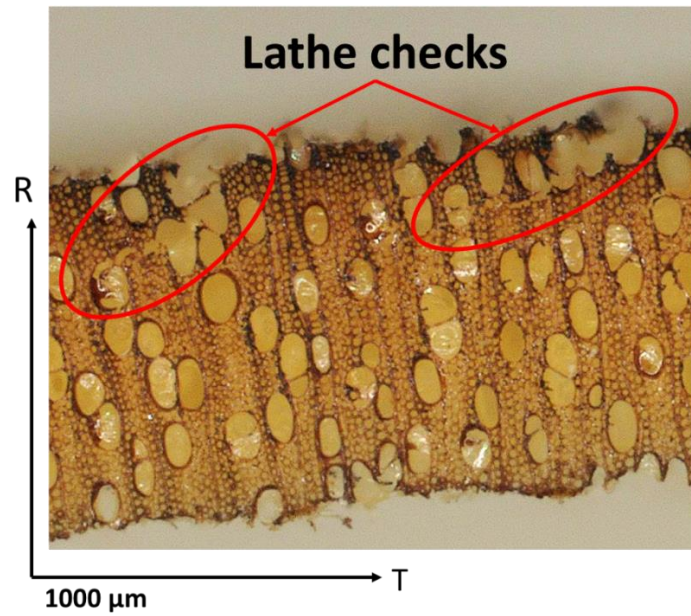
Figure 2- DCB specimen configuration for $0^\circ/0^\circ$ interface (top) and $0^\circ/90^\circ$ interface (bottom)



686

687

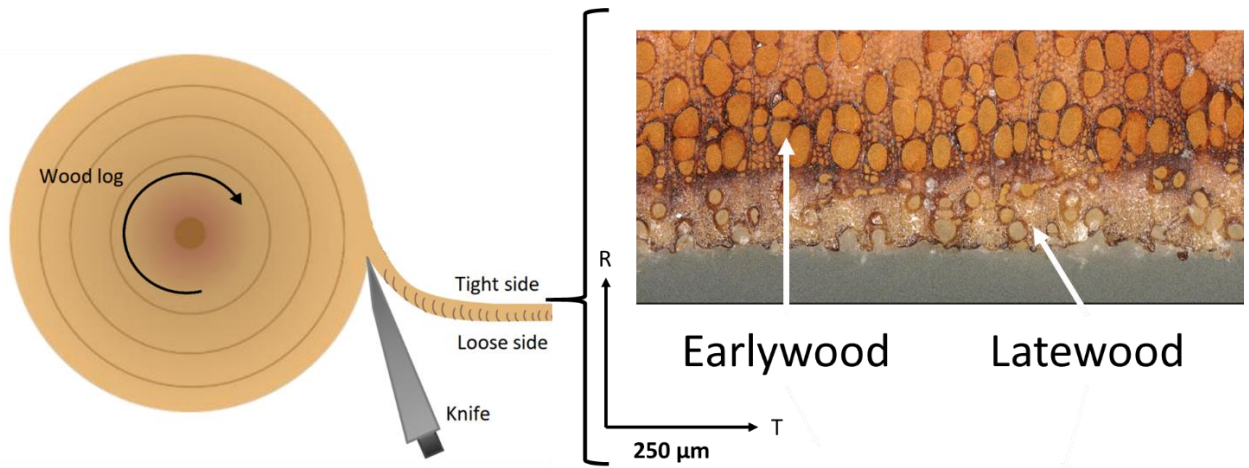
Figure 3- Microscope visualization of 0°/90° specimen thickness



688

689

Figure 4- Visible lathe checks on the poplar ply



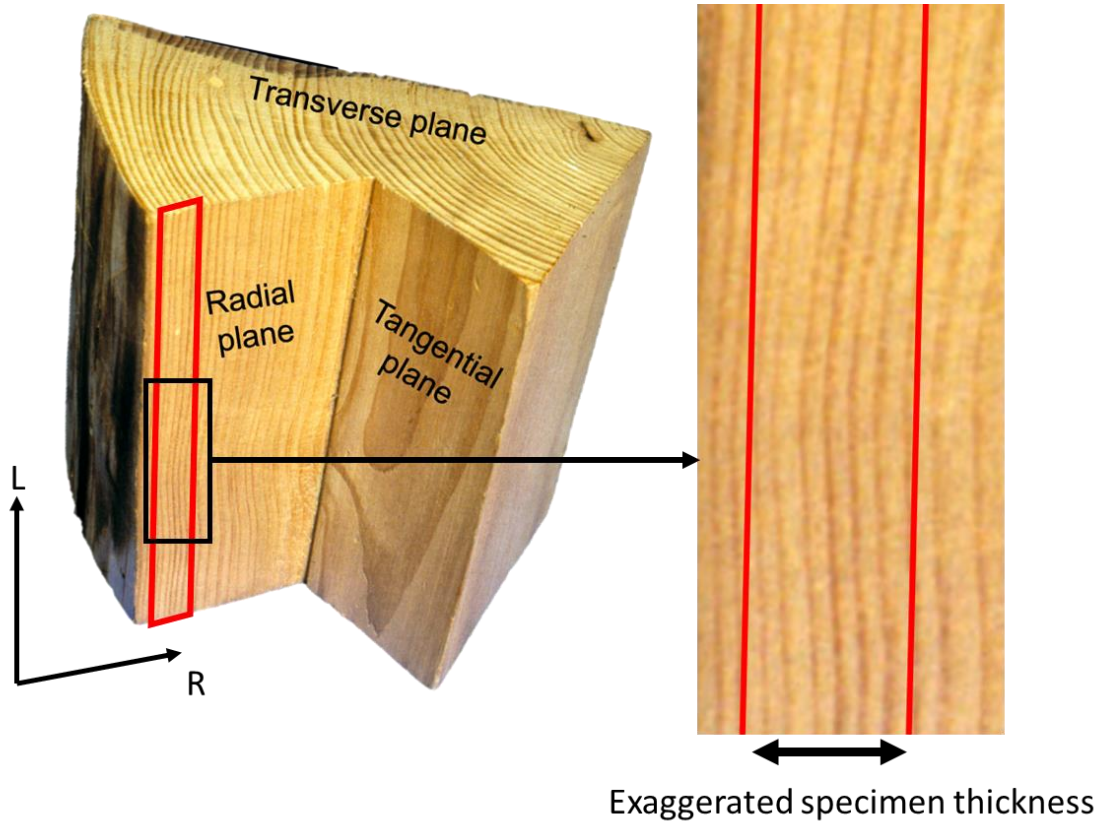
690

691

Figure 5 – Illustration of the veneer production process (left) [73] and a microscopic view of

692

earlywood and latewood on veneers (right)

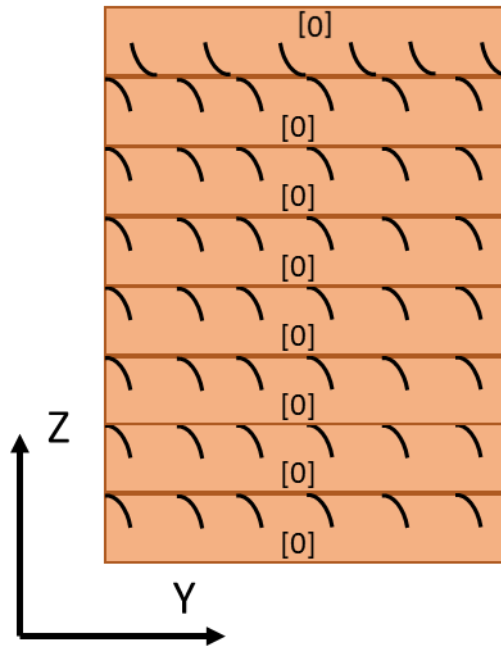


693

694

Figure 6 – An exaggerated representation of veneer LR plane on a wood log [74]

695

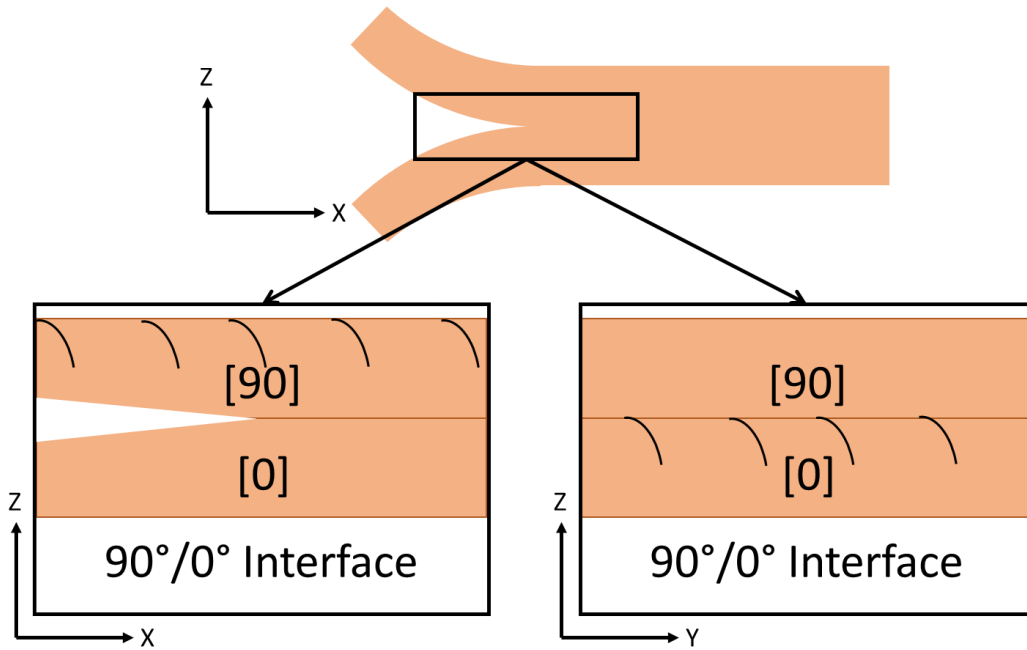


696

697

Figure 7- Stacking of the veneer of DCB 0°/0° specimens

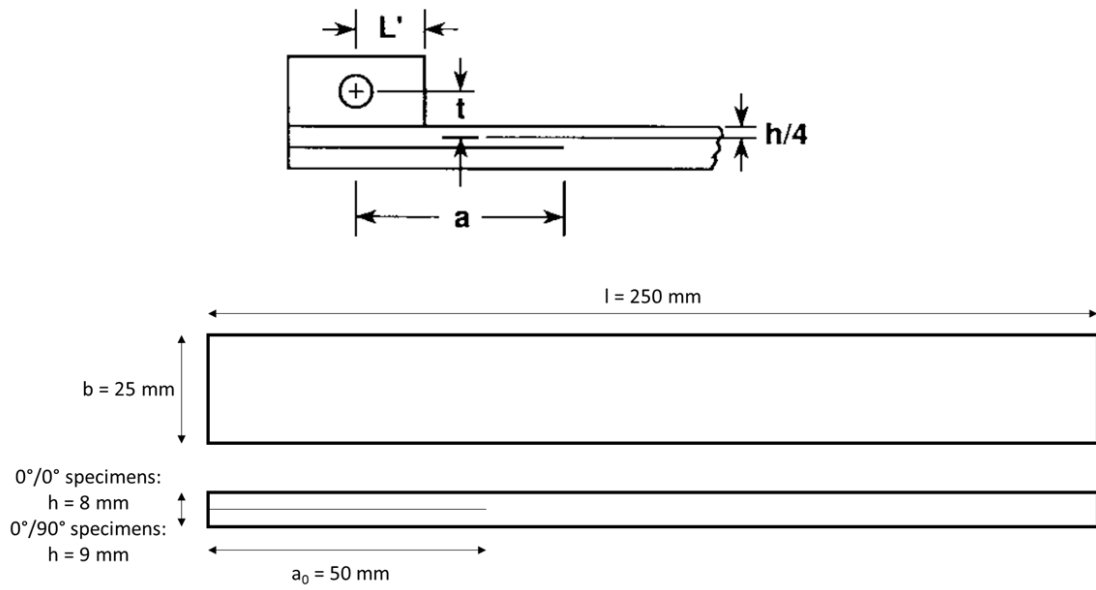
698



699

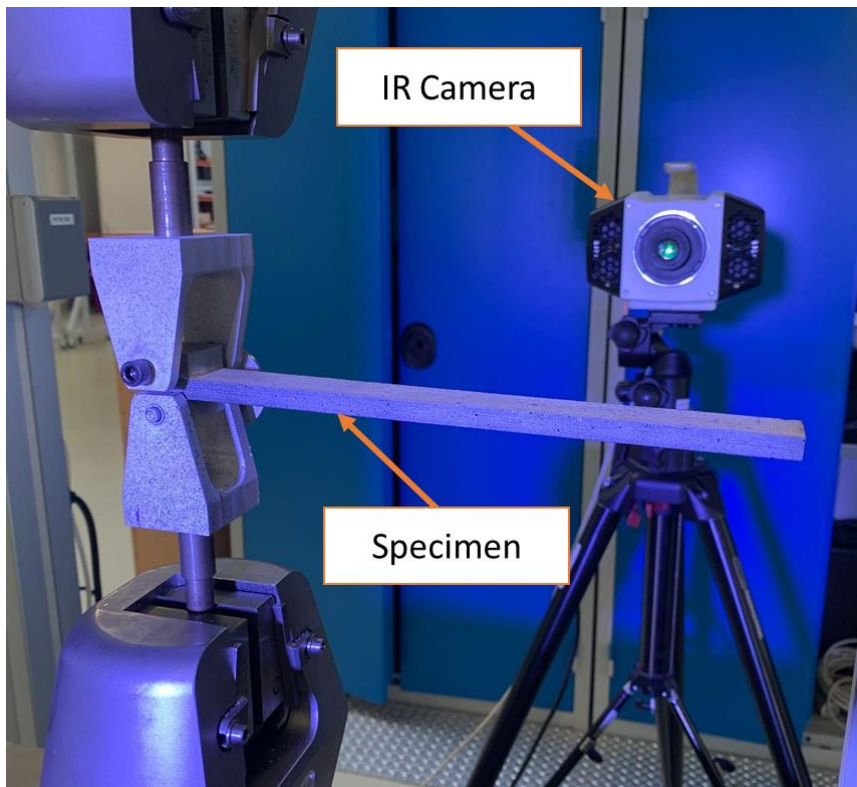
700

Figure 8- Stacking of the veneer at the interface of DCB 0°/90° specimens



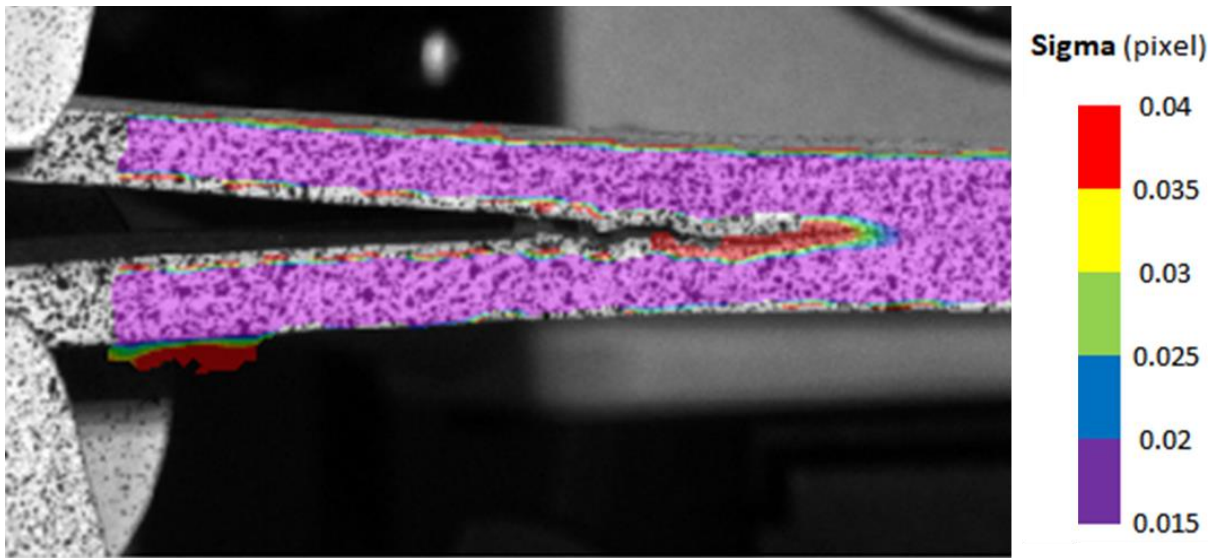
701
702

Figure 9- DCB specimen shape used in the experiments



703
704

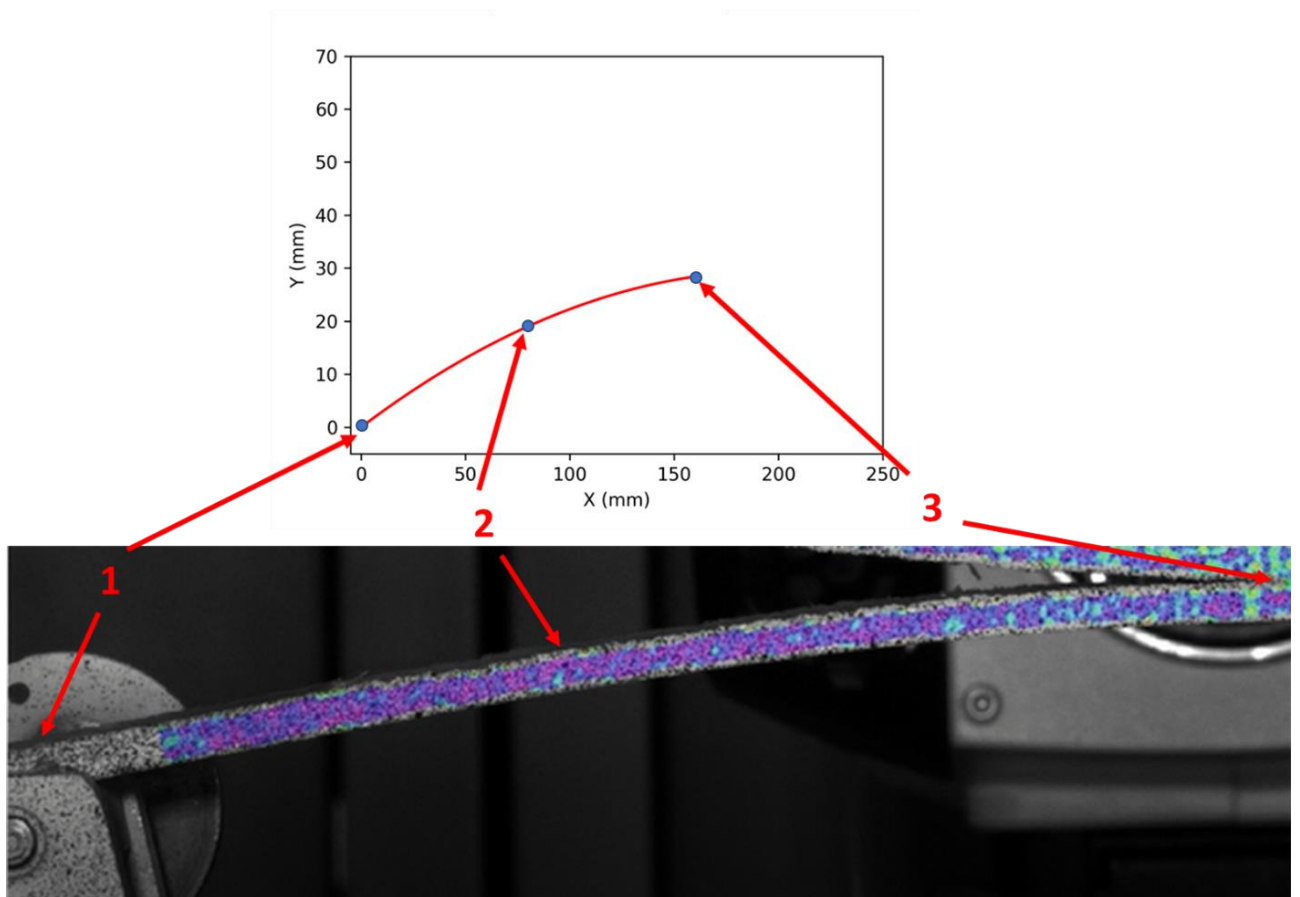
Figure 10- Experimental Setup used during the DCB test



705

706

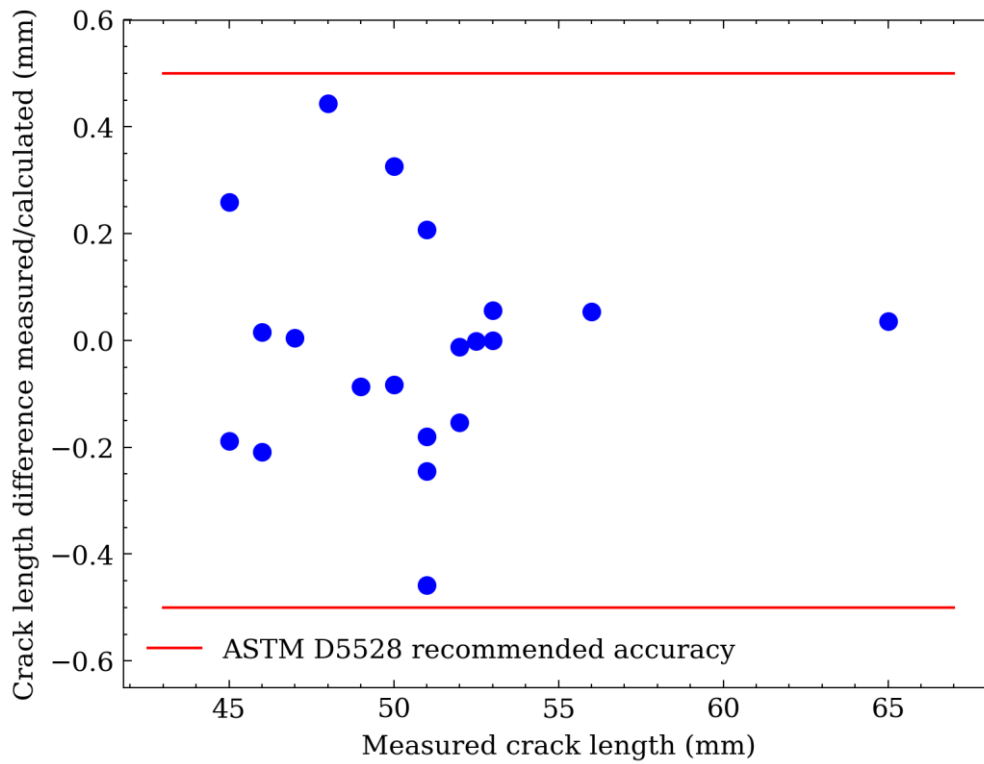
Figure 11 – Sigma visualization for one 0°/90° specimen (Colored figure)



707

708

Figure 12 – Three-point interpolation used to obtain the crack length (Colored figure)



709

710

Figure 13 – Difference between measured and calculated initial crack length



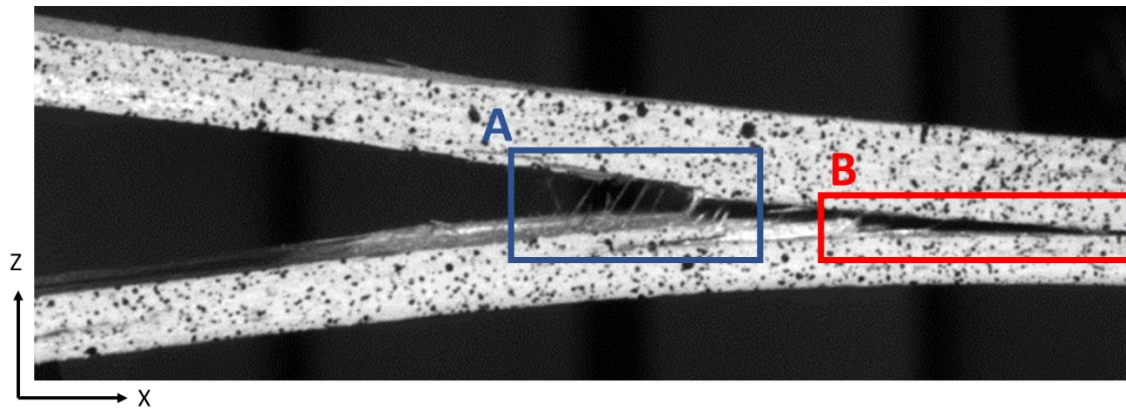
711

712

Figure 14 – Illustration of the crack path leaving the interfacial $0^\circ/0^\circ$ due to fiber out-of-plane

713

angle

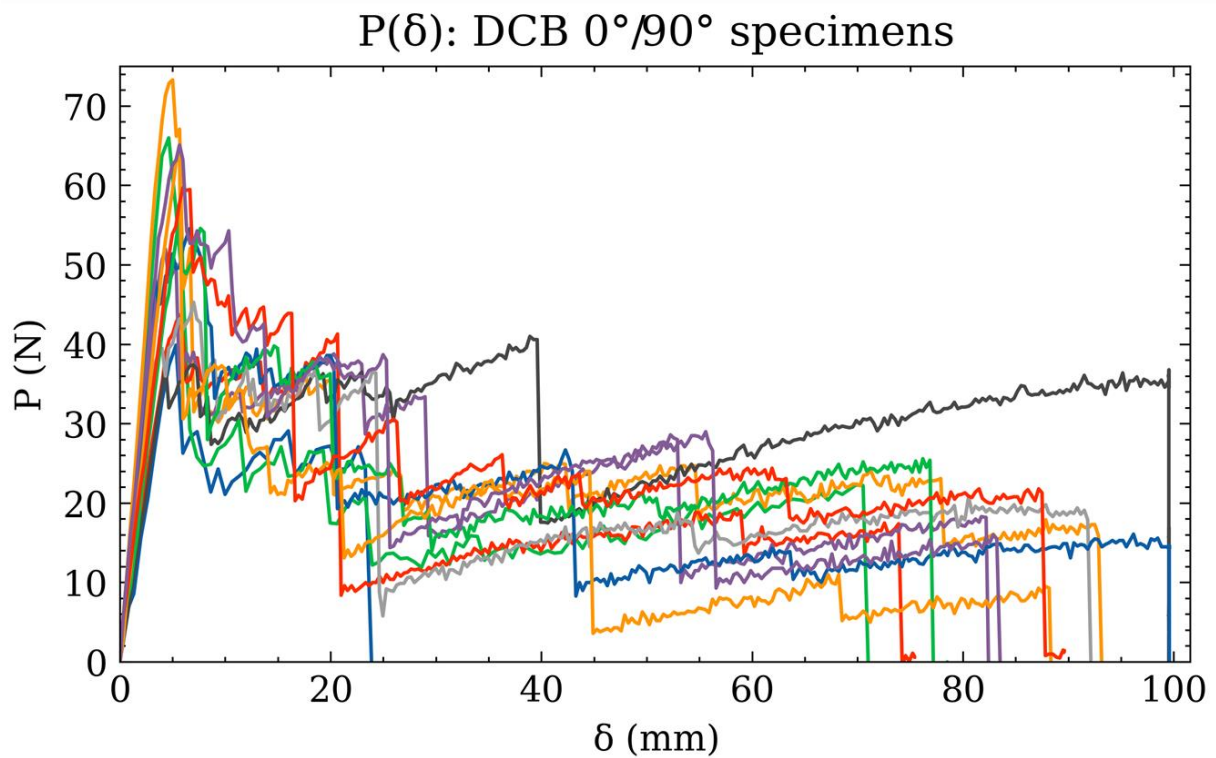
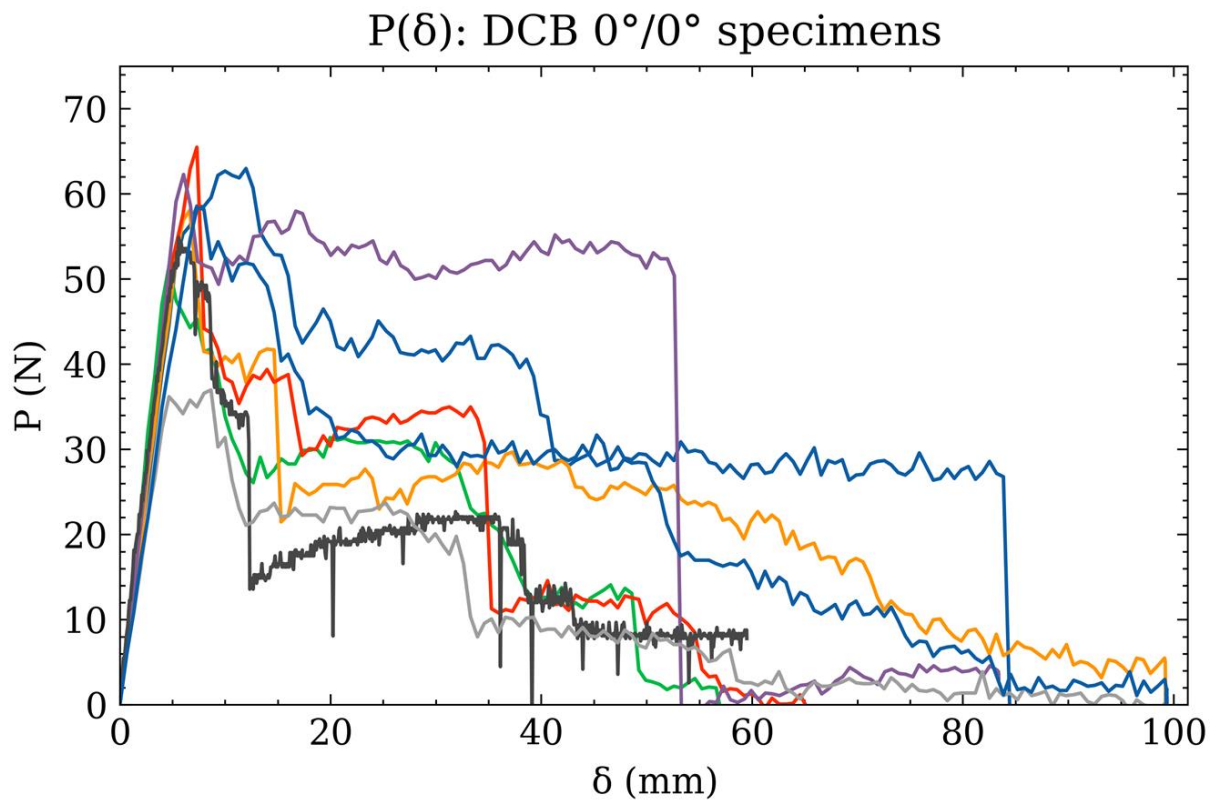


714

715

716

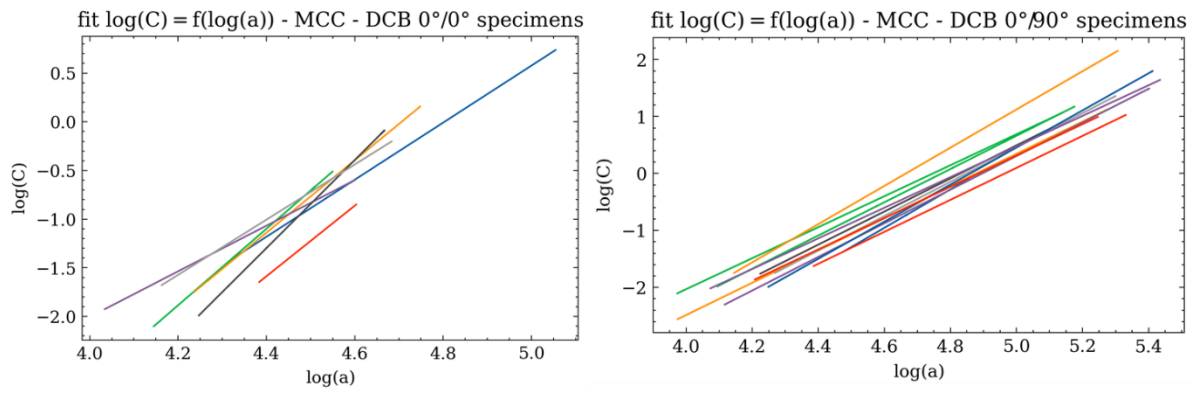
Figure 15 – Post-mortem of specimen $0^{\circ}/0^{\circ}$ no. 4 with fiber bridging (A) and crack that has migrated out of the initial interface (B)



717

718

Figure 16- P - δ curves for $0^\circ/0^\circ$ specimens (top) and $0^\circ/90^\circ$ specimens (bottom)

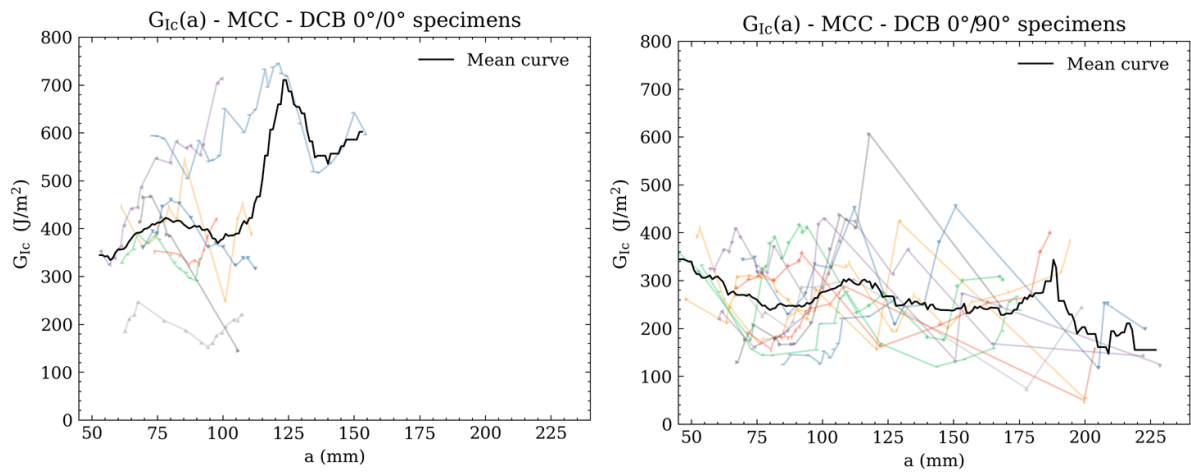


719

720 **Figure 17 – Fit calibration with MCC method for 0°/0° specimens (left) and 0°/90° specimens**

721

(right)

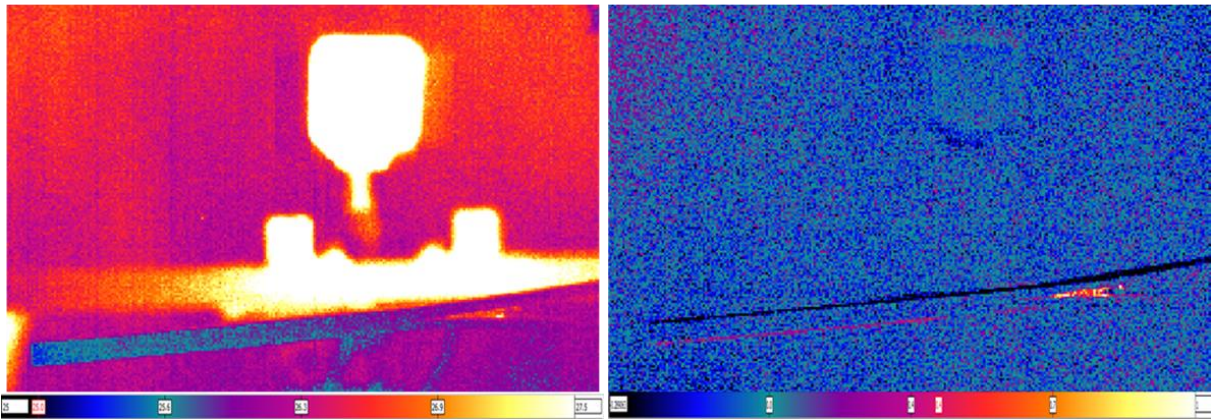
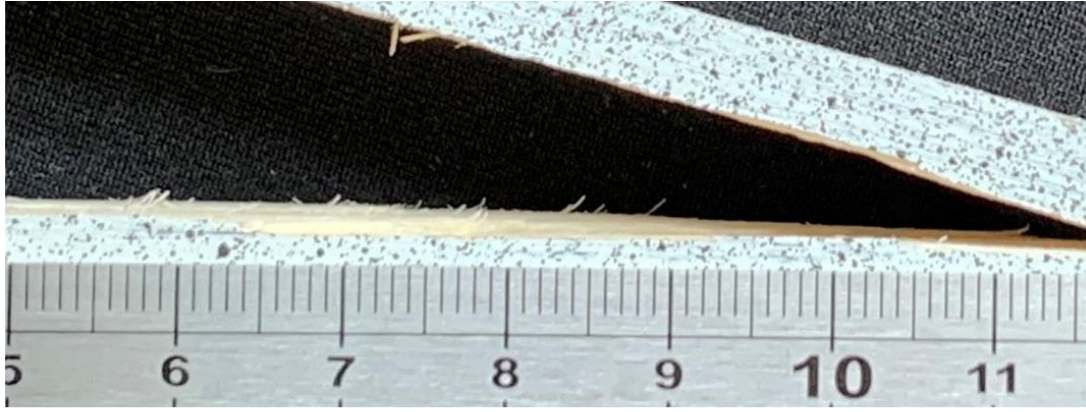


722

723 **Figure 18 – R-curves for 0°/0° specimens (left) and 0°/90° specimens (right) with the mean curve**

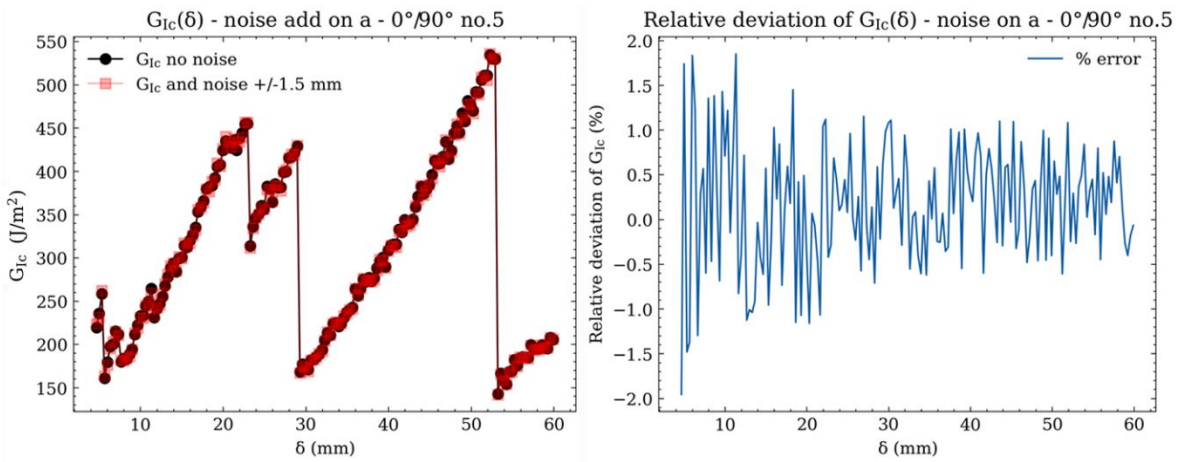
724

(20-point rolling mean)



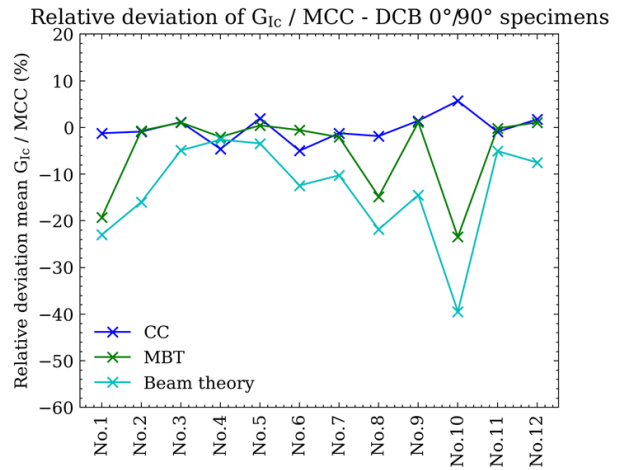
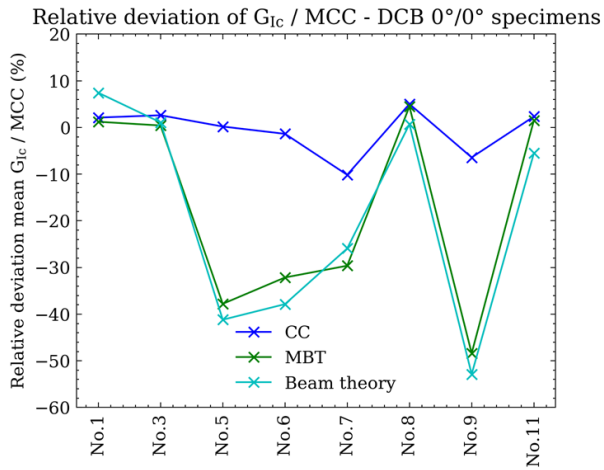
725
726
727
728

Figure 19 – Close-up view of broken fiber (top), IR camera capture (bottom left) and the difference between two consecutive images (bottom right)



729
730
731
732

Figure 20 – G_{Ic} with and without noise added to the crack length measurement (left) and relative difference between G_{Ic} with and without noise added to the crack length measurement (right) on specimen 0°/90° no. 5



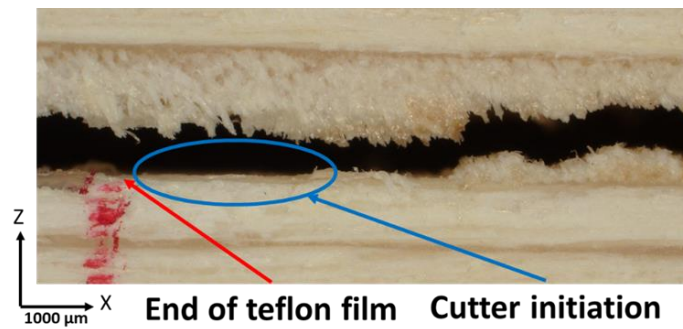
733

734

Figure 21 – Relative deviation of G_{Ic} methods compared to the MCC method for $0^\circ/0^\circ$ specimens

735

(left) and $0^\circ/90^\circ$ specimens (right)



Glued interfaces



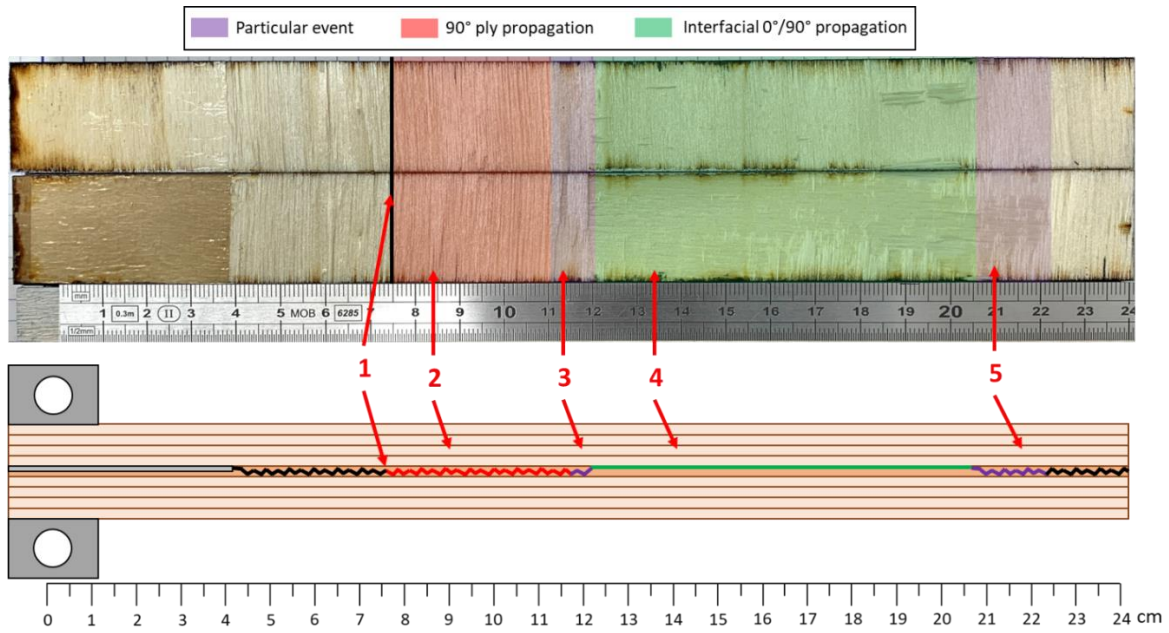
736

737

Figure 22 – Initiation and intra-ply migration (top) 90° ply; intra-ply crack propagation in

738

$0^\circ/90^\circ$ specimen (bottom)



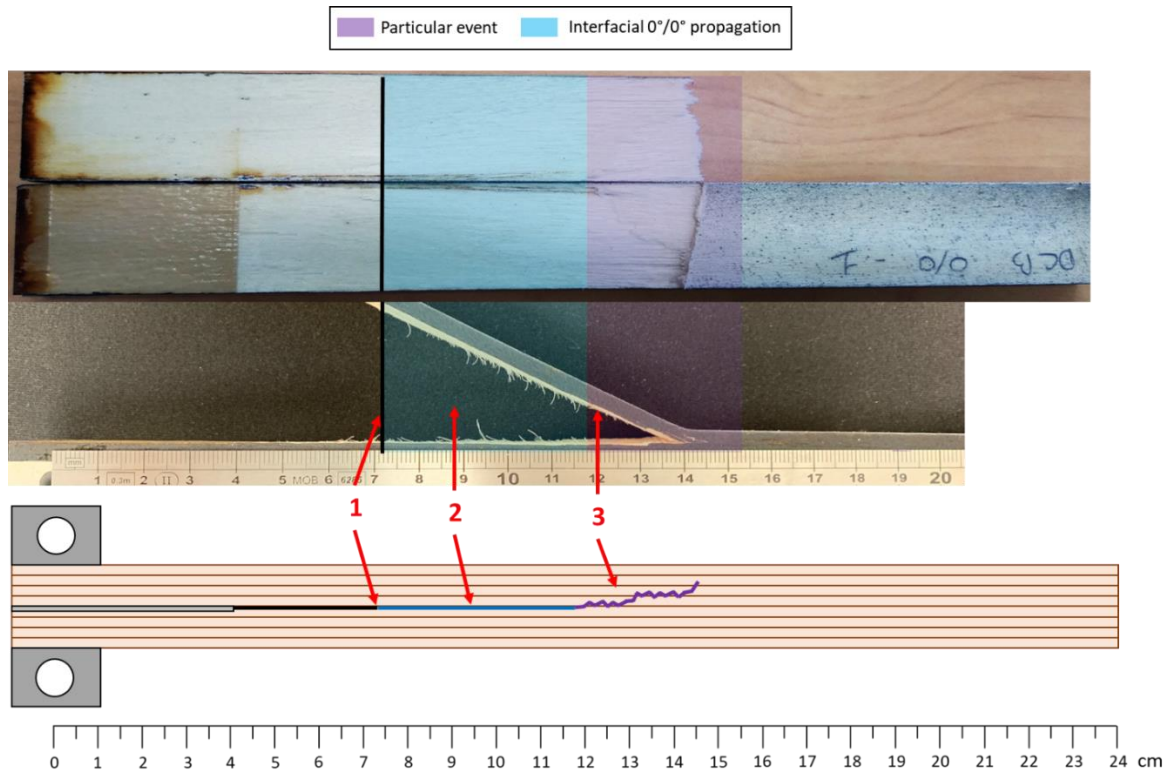
739

740

741

742

Figure 23 – Post-mortem examination of upper and lower interfaces of specimen 0°/90° no. 4 with identification of propagation zones (top) and illustration of the crack path and propagation zones through the same specimen (bottom) (Colored figure)

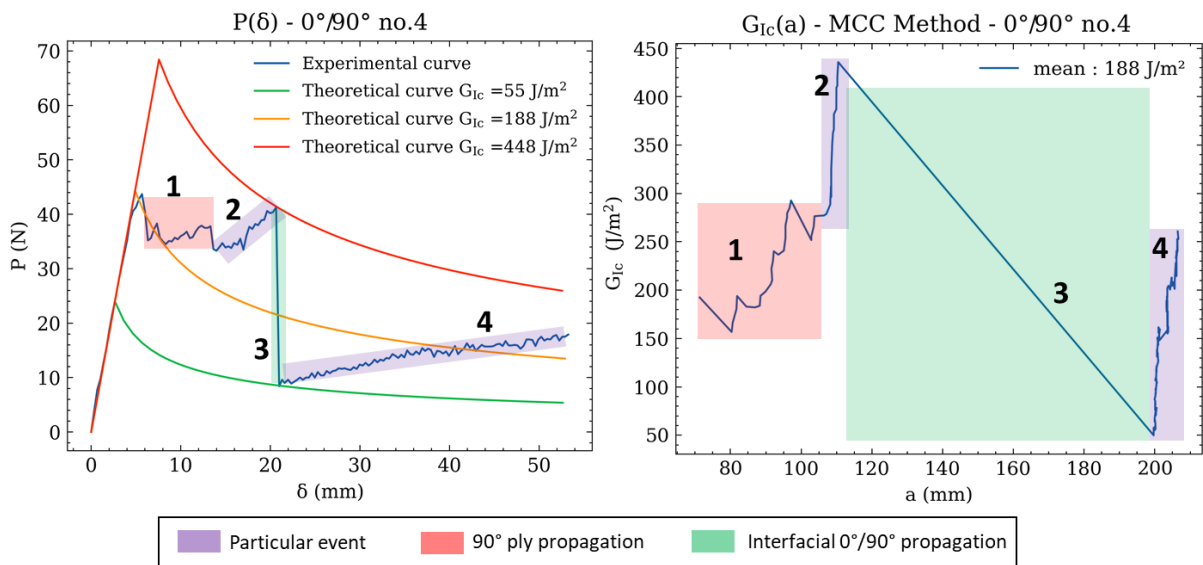


743

744 **Figure 24 – Propagation zones (top) and illustration of the crack path (bottom) for the specimen**

745

0°/0° no. 1 (Colored figure)

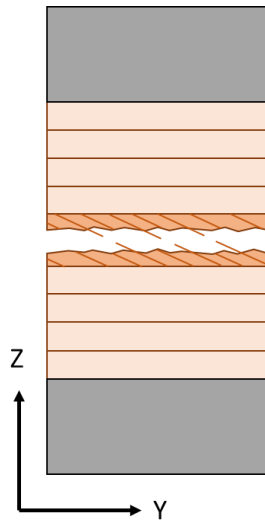


746

747 **Figure 25 – Experimental and theoretical P-δ curves (left) and R-Curve (right) for the specimen**

748

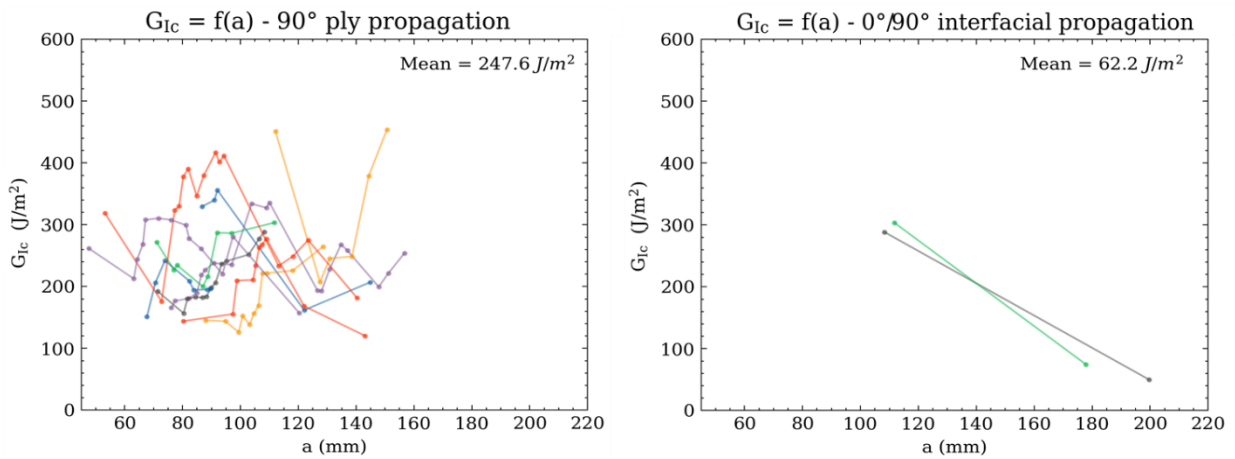
0°/90° no. 4 (Colored figure)



749

750

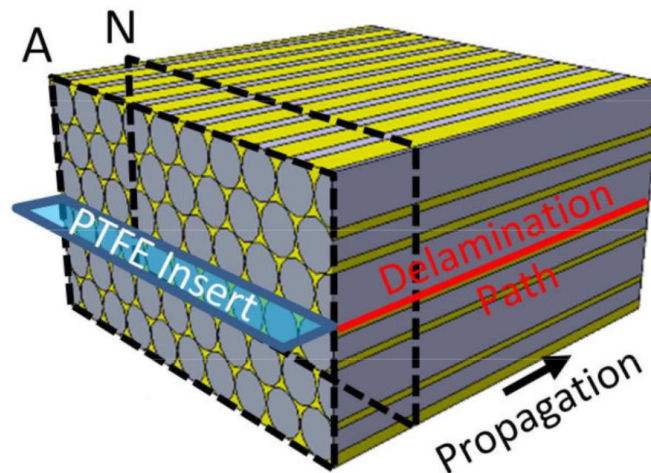
Figure 26 – Out-of-plane fiber bridging on 0°/90° specimens



751

752

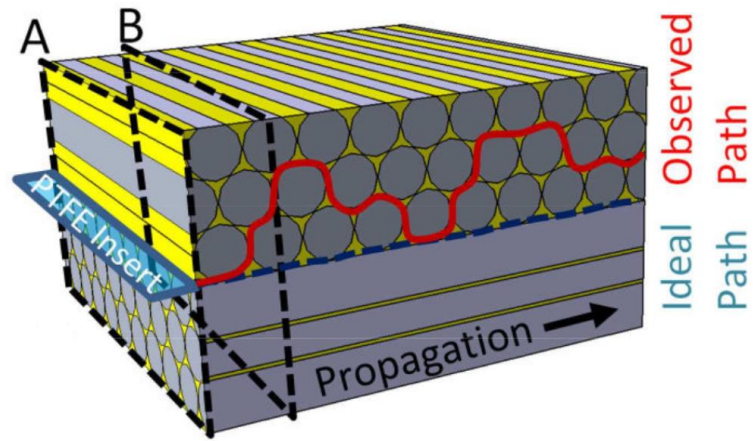
Figure 27 – $G_{Ic}=f(a)$ by propagation zones for 0°/90° specimens



753

754

Figure 28 – Expected delamination path for a 0°/0° interface [50] (Colored figure)



755

756

Figure 29 – Expected delamination path for a $0^{\circ}/90^{\circ}$ interface [50] (Colored figure)

757

Conflict of Interest Form

758 The authors declare that they have no known competing financial interests or personal relationships
759 that could have appeared to influence the work reported in this paper.